PERFORMANCE CHARACTERIZATION OF SILICON-ON-INSULATOR (SOI) CORNER TURNING AND MULTIMODE INTERFERENCE DEVICES

By

Qi Zheng

A thesis submitted to the
Faculty of Graduate and Postdoctoral Studies
in partial fulfillment of the requirements for the degree of
Master of Applied Science

Ottawa-Carleton Institute of Electrical and Computer Engineering
School of Electrical Engineering and Computer Science
Faculty of Engineering
University of Ottawa

July 2012

ACKNOWLEDGMENTS

First of all, I would like to express my great gratitude towards my thesis advisor Professor Trevor J. Hall for providing me the research environment, continuous support, valuable directions and superb guidance throughout this work. He has been a source of constant encouragement and enthusiasm. Without his trust and encouragement, this work would have never been possible.

I would also like to thank the following people, who are current or former members of Photonic Technology Laboratory at the School of Electrical Engineering and Computer Science, University of Ottawa: Prof. Henry Schriemer, Dr. Degui Sun, Dr. Sawsan Majid, Dr. Imad Hasan, Dr. Wei Yang, Dr. Kaisar Khan, Dr. Vahid Eslamdoost, Dr. Ramon Maldonado-Basilio, Dr. Akram Akrout, Erin Knight, Robert Radziwilowicz, Kais Dridi, Julie Udoeyop, Ali Hussein, Ran Li, Hamdam Nikkhah and Amanda Carr. Their strong supports and generous help greatly improved my research work. I will always cherish the good memories of working with them.

Finally, I am greatly indebted to my parents and beloved husband, for their immeasurable love and the biggest support, physically and mentally, to my study.

TABLE OF CONTENTS

LIST OF FIGURES

LIST OF TABLES

ABSTRACT

Silicon-on-insulator (SOI) technology has become increasingly attractive because of the strong light confinement, which significantly reduces the footprint of the photonic components, and the possibility of monolithically integrating advanced photonic waveguide circuits with complex electronic circuits, which may reduce the cost of photonic integrated circuits by mass production.

This thesis is dedicated to numerical simulation and experimental performance measurement of passive SOI waveguide devices. The thesis consists of two main parts. In the first part, SOI curved waveguide and corner turning mirror are studied. Propagation losses of the SOI waveguide devices are accurately measured using a Fabry-Perot interference method. Our measurements verify that the SOI corner turning mirror structures can not only significantly reduce the footprint size, but also reduce the access loss by replacing the curved sections in any SOI planar lightwave circuit systems. In the second part, an optical 90^{o} hybrid based on 4 × 4 multimode interference (MMI) coupler is studied. Its quadrature phase behavior is verified by both numerical simulations and experimental measurements.

CHAPTER 1 INTRODUCTION

1.1. Background Review of Silicon Photonics

Silicon photonics is a fast-growing area that studies different photonic systems using silicon, which is the dominant material in the microelectronic industry, as the platform for the generation, propagation, manipulation, and modulation of optical waves [1-4]. Silicon photonics offers a promising solution for monolithic integration of optics and microelectronics components at a common chip-scale platform for applications of high-speed optical interconnects in a small footprint.

Study of silicon photonics is motivated by the requirement of energy-efficient and high-speed interconnects to transport information. The use of high-index contrast silicon-on-insulator photonic waveguides in interconnects is very promising, as pure silicon has very low material absorption losses at telecommunications spectral range (~1550 nm), and a silicon photonic waveguide interconnect could have higher bandwidth, smaller footprint, shorter interconnect delays and more importantly, full compatibility with the CMOS process used for fabricating electronic devices. Therefore, integration of optical and electrical devices on a single chip is made possible.

Pioneering works on silicon photonics can be traced back to the late 1980s and early 90s [5-7] and substantial progress has been made since then. Using silicon as a photonic material usually has some difficulties, such as the high propagation losses, low electrooptic coefficient, low light-emission efficiency and high coupling loss with fiber devices. Great efforts have been

directed to overcome these traditional limitations thanks to development of high performance integrated photonic components, which are made possible by the recent progress in nanofabrication techniques.

Low loss silicon waveguides are important for on-chip optical networks. Propagation losses in silicon photonic waveguides are mainly from power coupling to radiation modes and scattering due to imperfections in the fabrication of the waveguides. In the telecommunication wavelength band at around 1550 nm, intrinsic absorption in the silicon material can be neglected [8]. Low-loss single-mode silicon optical waveguides with sub-micron size dimensions have been demonstrated with propagation losses less than 3 dB/cm in 2004 [9], which is made possible owing to the small sidewall surface roughness achieved by processing on a 200mm CMOS fabrication line. For submicron size strip waveguides, the lowest loss reported to data in the 1550 nm spectral range is around 1 dB/cm [10]. The losses, due to both scattering at the waveguide sidewalls and absorption, originate mainly from the etching process. In order to minimize the losses of silicon waveguide, most recently, etchless process based on selective oxidation has been used to fabricate low loss silicon photonic waveguide with losses as low as 0.2-0.3 dB/cm at 1550 nm band [11, 12].

The high fiber-to-waveguide coupling losses originate from the mode area mismatch between the fiber (~10 um diameter) and silicon waveguide (<1 um diameter). Tapering structures from the fiber dimensions to the waveguide dimensions for improving fiber-to-waveguide coupling efficiency have been demonstrated as well [13]. Propagation modes in an optical fiber with cross-sectional dimensions of several of micrometers can be converted down to only a few hundreds of nanometers in a silicon waveguide in a very short length.

Another feature of silicon photonic waveguides is that the high optical intensity arising from large index contrast caused strong light confinement enables strong nonlinear optical interactions, such as Raman and Kerr effects, in chip-scale devices. As a result, optical amplification, light emission, and modulation functions are all made possible [2]. In the past a few years, great efforts in silicon photonics have been directed to active silicon photonic devices, such as modulators, amplifiers, and light emitters.

Since the linear electrooptic effect is absent in silicon material due to its centro-symmetric crystal structure, silicon is usually difficult to achieve electrooptic modulation. To solve this problem, progress has been made in the past decade. Different geometries in silicon have been investigated to achieve high-speed electrooptic modulation. For example, silicon-based optical modulators operating at more than 10 Gbs/s have been demonstrated based on metal-oxide-semiconductor capacitors [14, 15]. The most common method of achieving fast modulation in silicon photonic devices is to exploit the plasma dispersion effect, which is related to the concentration of free carrier in silicon and changes both the real and imaginary parts of the refractive index [16]. Silicon modulators using the plasma dispersion effect working at 40Gb/s have been demonstrated recently based on a traveling wave design [17]. However, the change of refractive index is associated by a detrimental change in optical intensity due to the absorption of free carriers. In order to achieve more efficient modulation, alternative mechanisms have been investigated using other materials that are potentially compatible with silicon technology [18].

It is well known that silicon has an indirect band gap structure, which leads to a poor optical-emission efficiency. While silicon has many limitations as a light emitter, many efforts have been made to enable light emission in silicon [19-24]. To increase the light emission efficiency

of silicon and to achieve optical gain, different techniques have been developed, including those based on decreasing the radiative lifetime with respect to the nonradiative processes using quantum confinement by nanocrystals [25] or stimulated Raman scattering [26, 27] and those using the silicon as a host material for erbium doping [28]. On the other hand, due to the huge obstacles imposed by the silicon material characteristics, hybrid silicon lasers have been demonstrated to show promising and advanced device functionality [24]. A hybrid silicon laser usually bonds compound semiconductor materials to a silicon-on-insulator substrate [29]. The former provides the necessary optical gain for lasing, while the latter serves as the optical waveguide to guide the emitted optical mode.

In a word, thanks to the recent progress in nanofabrication techniques, novel mechanisms have been developed for achieving both passive and active ultracompact silicon devices with high performance. On the other hand, there is immediate need for silicon photonics in integrated high-speed optical interconnects. Silicon photonics is bringing us a bright future for commercial integrated optoelectronics.

1.2. Fundamentals of Silicon Photonic Waveguides

The fundamental building block of the photonic circuits is a waveguide. The simplest optical waveguide is the step-index planar waveguide. Since a planar waveguide confines the light beam in one dimension only and therefore is a 1D waveguide. The study on silicon photonic waveguides also started with planar waveguides [30]. As shown in Figure 1.1, a silicon planar waveguide consists of a high-index silicon layer surrounded by other materials with lower refractive index on both sides. Therefore the optical field can be confined in the silicon core

layer. A silicon planar waveguide has a simple three-layer structure and hence an analytical solution of the waveguide equation exists [31].

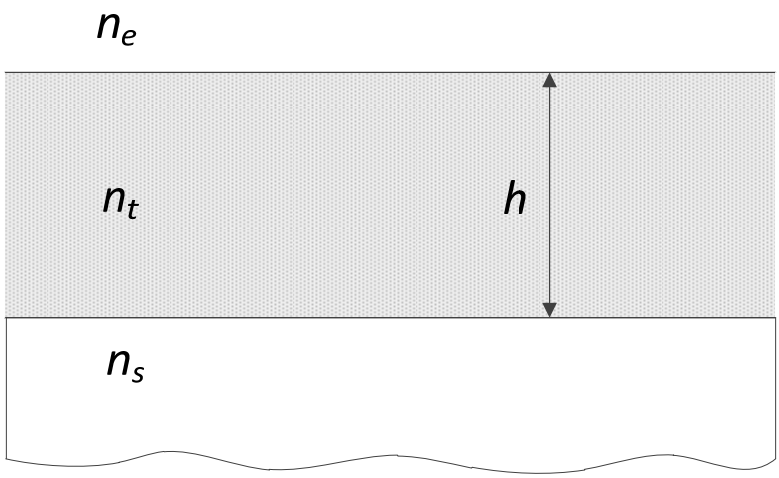

Figure 1.1 Silicon planar (slab) waveguide.

Despite the simple structure, the utility of the silicon planar waveguide is very limited in applications because light is confined in one dimension only. For many practical applications, two-dimensional photonic waveguide for optical wave confinement is required, which can be achieved in silicon by etching a two-dimensional waveguide. Several types of two-dimensional photonic waveguides with different geometries and light guidance mechanism have been investigated in silicon.

The most commonly used silicon photonic waveguides are channel (or strip) waveguides and ridge (or "rib") waveguides, as shown in Figure 1.2. In channel waveguides, the core layer, which guides the light wave, is completely surrounded by a cladding layer with higher refractive index (Figure 1.2a). Another type of waveguide similar to channel waveguides is silicon buried waveguides [32]. In rib waveguides, a dielectric ridge structure sits on top of a slab layer, forming the guiding layer, which is embedded between two low-index layers: the

bottom substrate layer and the top cladding layer, as shown in Figure 1.2b. It is obvious that optical confinement in the vertical direction is achieved by the refractive index difference between the guiding layer and the two cladding layers. On the other hand, the ridge structure has a slightly higher refractive index than that of the slab layer. Therefore, the rib structure can also achieve optical confinement in the lateral direction.

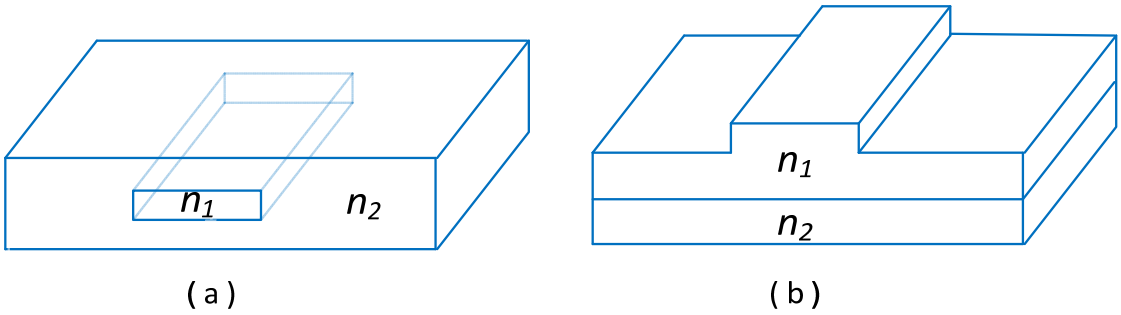

Figure 1.2 Configurations of silicon photonic waveguides: (a) channel waveguides, (b) ridge waveguides.

In both the channel and the rib silicon photonic waveguides, light is confined and guided thanks to the total internal reflection (TIR) between high-index core layer and the low-index cladding layers. The typical cross-sectional dimensions of these two types of waveguides are determined by the effective refractive index in the guiding layer. Cross-sectional diameters of channel waveguides are usually less than one micrometer (submicron). Ridge waveguides typically have a relatively large mode area (a few micrometers). Silicon waveguides with large cross-sectional sizes are usually used in relatively short straight (no bends) integrated photonic circuits due to their large bending loss. One advantage is that they are easier to couple light to the fibers. For integrated devices that require longer lengths, silicon waveguides with smaller cross-sectional dimensions are usually preferred and ultracompact devices integrated on single-chip are hence made possible.

Both the channel and rib waveguides are confining and guiding light based on the mechanism of TIR. In fact, light can also be confined in low-index-of-refraction regions in a silicon platform, thanks to its especially high refractive index. Two examples of such novel waveguides are photonic crystal waveguides and slot waveguides, as shown in Figure 1.3(a) and (b), respectively.

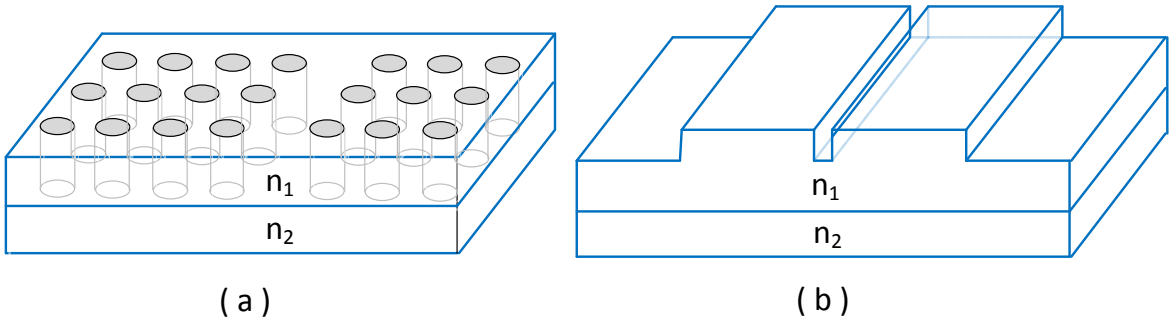

Figure 1.3 Configurations of two novel silicon photonic waveguides where light is confined in a low-index-of-refractive area: (a) photonic crystal waveguides, (b) slot waveguides.

Photonic crystals, with their name borrowed from the semiconductor crystals, refer to periodic dielectric structures consisting of alternating regions of dielectric materials with high and low refractive index. Since the periodicity is on the order of the wavelength of light, photonic crystals can be designed to affect the motion of photons in a similar way that semiconductor crystals affect the motion of electrons [33]. That is, the periodicity of dielectric structures produces a high reflection of light in a specific spectral range because the light cannot propagation in the crystal structure, which is similar to the energy gap in a semiconductor crystal. Thanks to its high refractive index, silicon is an ideal platform to create photonic crystals with complete band gaps (very high reflectivity) [34]. Therefore, a photonic crystal waveguide can be created by surrounding a channel waveguide with a two-dimensional photonic crystal region. The photonic band gaps force the light to be concentrated in the channel

waveguide, no matter how low its refractive index is. The photonic crystal waveguides are usually fabricated by removing materials from a complete periodic two-dimensional photonic crystal to create the channel waveguide. Due to the strong light confinement by the photonic bad gaps, photonic crystal waveguides can guide light in cores with very small dimensions.

A silicon slot waveguide is another new type of waveguide, where light can be also confined in a low-refractive-index region [35]. As shown in Figure 1.3b, the slot waveguide is formed by embedding a low-index slot between two high-index silicon waveguides with small cross-sectional dimensions (silicon wires). The light guiding principle is based on the overlap of the evanescent tails of the modes in two silicon wires. By using this new waveguiding mechanism, silicon waveguides can be shrunk to very small dimensions (less than 50 nm) [35], opening new application areas, such as evanescent sensors in biological or chemical fields [36].

1.3. Organization of the Thesis

This thesis is concerned with performance evaluation of two passive silicon photonic devices in silicon-on-insulator structures, specifically corner turning mirror and multimode interference (MMI) coupler. The organization of the thesis is as follows:

Chapter 2 "*Silicon-on-Insulator (SOI) Waveguide Device*" serves as a background review of SOI technology and the recent advances in SOI-based functional devices. The major numerical analysis methods of SOI waveguides are described. The sources of losses in SOI waveguides are also introduced, followed by a detailed description of commonly used techniques for measurement of propagation losses in SOI waveguides.

Chapter 3 and 4 present simulation and experimental results of two passive SOI-based devices, namely corner turning mirror and multimode interference coupler. In Chapter 3 "*Silicon-on-Insulator Rib Waveguide Corner Turning Mirrors*", a new type of SOI waveguide corner is investigated. Numerical simulations using finite-different time-domain method are first presented, followed by a detailed experimental testing. Comparison between corner turning mirrors and the conventional curved waveguides is also presented. Chapter 4 "*Silicon-on-Insulator Multimode Interference (MMI) Coupler*" studies the design, simulation and experimental demonstration of multimode interference couplers, and their specific utility as a 90^{o} optical hybrid for applications in radio-over-fiber links.

Finally in Chapter 5 "*Conclusions*", a summary of the main contributions of this thesis is presented. Suggestions of the potential improvements to the device design and the future work are also included.

CHAPTER 2 SILICON-ON-INSULATOR (SOI) WAVEGUIDE DEVICE

Silicon-based integrated circuits have find extensive applications in the fields, such as computers, wireless communications devices, and other electronic devices that widely used in our everyday life. In the past few decades, the high-index contrast "Silicon-on-insulator (SOI)" platform has attracted intensive interests thanks to its potential in further downscaling the integrated device size via monolithic photonic integration technique [37].

SOI technology uses a layered silicon-insulator-silicon substrate in place of conventional silicon substrates in semiconductor manufacturing. By this means, the parasitic device capacitance is reduced and the performance of the device can be greatly improved. Since the first industrial implementation of SOI by IBM [38], SOI technology has found numerous applications within the field of photonic integrated circuits (PIC). Both passive and active PIC components have been achieved on the SOI platform, such as Fabry-Perot microcavity-based resonators, micro-switches, modulators, lasers, photo-detectors, and arrayed waveguide gratings (AWG) [14, 39-42]. The key features of SOI technology include its compact confinement due to the high refractive index contrast of SOI waveguides between silicon layer and silica insulator substrate and good compatibility with the modern micro-electronics.

2.1. Introduction to SOI Waveguides

As its name implies, an SOI waveguide usually consist of a high-refractive-index single-crystal silicon layer as the waveguide core and a low-refractive-index thin buried silicon dioxide

(insulator) as a bottom cladding. The upper cladding can be just air or the same silicon dioxide layer to reduce surface contamination and to provide electrical isolation. The pure silicon core layer has a material refractive index of $n_{Si} \approx 3.5$, which is much higher than that of the buried silicon dioxide cladding layer ($n_{Si0_2} \approx 1.5$). The refractive index contract between core and cladding layers in SOI waveguide is much higher that of other optical waveguides such as optical fibers, leading to tight confinement and guiding of light within a small scale core region (submicron). Such lateral and vertical dimensions are usually required for true compatibility with integrated circuits (IC) processing. This is the most distinct advantage of SOI waveguides over the other widely used waveguide platforms such as III-V semiconductor compounds and polymers. In addition, the large refractive index contrast between silicon and silicon dioxide causes the high optical intensity within the silicon core, which makes it easier to observe nonlinear optical interactions, such as Kerr and Raman effects. Silicon has superior material properties that benefit the nonlinear optical effects in SOI waveguides, include high thermal conductivity, high optical damage threshold, and high third-order optical nonlinearities.

Another feature of SOI technology is that silicon is not only used as the waveguide core material, but also as the waveguide substrate. Silicon material is an ideal platform for integrated electronic circuits. Therefore, SOI technology offers promising potential for monolithic integration of photonic devices with electronic devices on the same substrate. Moreover, thanks to the mature silicon fabrication technology developed for electronic devices, SOI technology enables low-cost fabrication of compact integrated photonic devices for mass-market applications.

Owing to the advantages of SOI technology listed above, various optical integrated devices have been realized so far on the SOI platform, including passive devices such as low-loss strip waveguides [43], efficient optical directional couplers [13], microring-resonator-based optical add/drop filters [44], nano-cavities [45], polarization splitters [46], and active devices such as optical modulators [47], optical switches [3] and light sources [27].

Different types of silicon photonic waveguides have been described in Chapter 1. An SOI wafer is a good example of a slab (planar) waveguide with a three-layer structure. Due to the high refractive index difference between the core layer of single-crystal silicon and a thin bottom cladding layer of buried silicon dioxide, the guided light propagating along the *z*-direction is confined tightly in the high index silicon core layer in the *y*-direction. The typical dimension of the silicon guiding layer is about a few micrometers in thickness, and the buried silicon dioxide layer is usually about a few hundred of nanometers in thickness. While the slab SOI guide has very simple structure, its practical use is very limited because light is confined only in one dimension (along *y*-direction).

More practical SOI waveguides usually provide two-dimensional confinement (both x-direction and y-direction) of the light propagating along z-direction. As has been discussed in Chapter 1, the two most commonly used two-dimensional SOI waveguides are strip and rib waveguides. Figure 2.1 shows the field (single-mode) distributions in both single-mode strip and SOI rib waveguides. Due to the strong light confinement in strip waveguides, a single-mode strip waveguide usually has a small dimension (a few hundred nanometers), which produce difficulties in waveguide fabrication and light coupling. On the other hand, a rib waveguide with much larger dimension (a few micrometers) can still support single-mode operation, which

greatly relaxes fabrication tolerances and makes the SOI rib waveguide the preferred platform in device design.

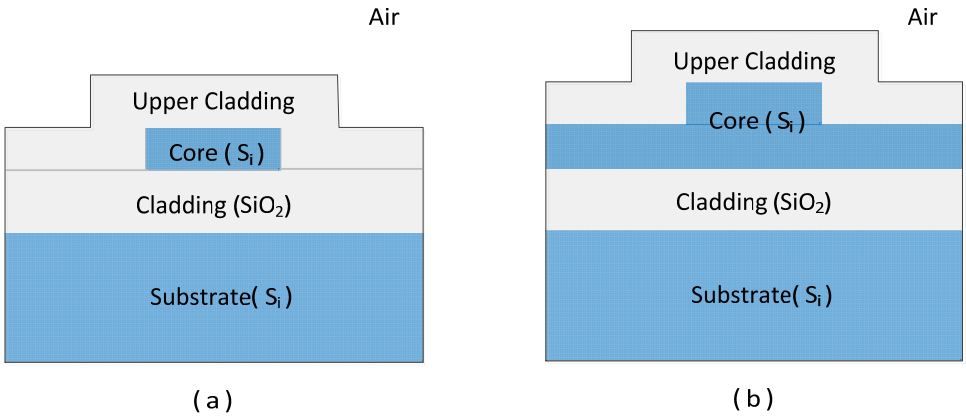

Figure 2.1 Cross-sections and single-mode operation of two commonly used SOI waveguide structures: (a) a strip waveguide, (b) a rib waveguide.

Based on the above concerns, in this thesis, all the waveguide devices are fabricated in SOI rib waveguides. In most applications of the SOI rib waveguides, such as sensor and interconnections systems, single-mode operation is usually required for the waveguides. Large-dimension single-mode SOI rib waveguides have been intensively investigated since late 1990s [48-50]. The numbers of optical modes that can be supported by a SOI rib waveguide is determined by its cross-section dimension geometry. A typical SOI rib waveguide is shown in Figure 2.2. The geometry of the rib waveguide is mainly defined by three parameters: the silicon rib with W, the total height of silicon core *H*, and the thickness of the silicon slab waveguide *T*. Note that a large dimension SOI rib waveguide cannot be truly single-mode. Some higher-order modes, other than the fundamental mode, may be excited. However, it has been demonstrated that, if the geometry of the SOI rib waveguide is correctly designed, the excited higher-order modes will leak out of the waveguide quickly over a very short

propagation distance, and only the fundamental mode can be propagated. With the geometry parameters defined in Figure 2.2, a large dimension SOI rib waveguide that supports single-mode operation can be determined by an approximate expression [49],

$$\frac{W}{H} \le 0.3 + \frac{T}{\sqrt{H^2 - T^2}} \qquad (for\ 0.5H < T < H) \tag{2-1}$$

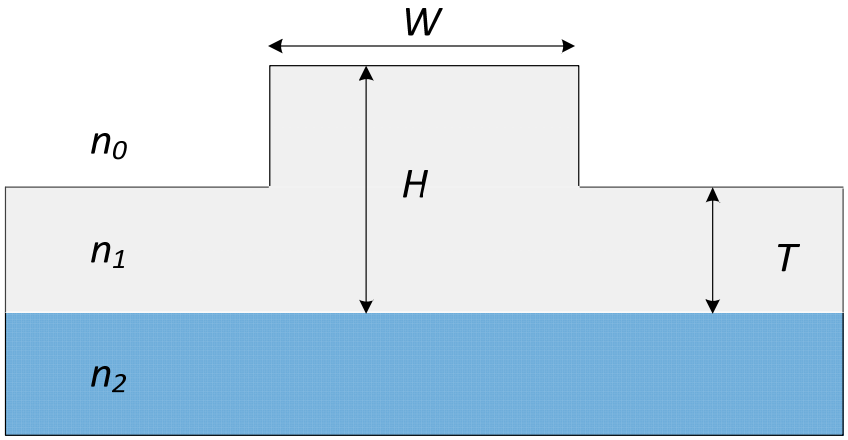

Figure 2.2 Geometry of a typical SOI rib waveguide: parameter definitions.

2.2. Methods of SOI Waveguide Analysis

Light propagation and electromagnetic fields in SOI waveguides can be obtained by solving the Maxell equations. For the simplest SOI slab (planar) waveguide with uniform refractive-index profile in the core layer, analytical eigen solutions (optical modes) exist. Considering that the guided electromagnetic fields are confined in the core layer and exponentially decay in the cladding layers, the electric field distribution can be uniquely determined by the propagation constants and the effective index of the guided modes [31]. Note that due to the one-dimensional light confinement, two orthogonally polarized modes can be supported in a slab waveguide: the transverse electric (TE) mode and the transverse magnetic (TM) mode. If the

electric field of an optical mode is perpendicular to the propagation direction and lies in the plane of core layer, it is called TE mode. On the contrary, TM mode refers to the optical mode with the magnetic field perpendicular to the propagation direction [31].

However, for a SOI waveguide with two-dimensional confinement, such as a strip or rib waveguide, no analytical eigen solutions exist for the Maxell equations. A varity of techniques have been used to analyze two-dimensional SOI waveguides. One solution is to use effective index method (EIM), which approximates a two-dimensional waveguide structure to a one-dimensional slab waveguide, and then an analytical solution can be obtained. While it is very simple, EIM method has approximated solutions and its applications limit in waveguides with simple geometrical cross-section structures. To accurately analyze SOI waveguides with complicated cross-sections, some numerical analysis methods are required, such as finite element method (FEM), finite different time-domain (FDTD), and beam propagation method (BPM). The following subsections describe the principles of the above widely-used analysis methods for SOI rib waveguides. In this thesis work, both FDTD and BPM methods have been used for numerical simulation of SOI waveguide devices.

2.2.1. Effective Index Method (EIM)

As its name implies, the effective index method (EIM) finds the approximate solutions for the propagation constants of supported modes in a two-dimensional waveguide by calculating the effective index of the waveguide. Consider a typical SOI rib waveguide shown in Figure 2.2. The EIM method treats the rib waveguide as a combination of two orthogonal planar waveguides, one horizontal and one vertical. The method is implemented in two steps. In the first step, the effective index of the first (horizontal) planar waveguide is obtained by solving

the planar waveguide eigenvalue equations. This procedure is implemented three times for three different parts of the waveguide: the left slab waveguide, the central rib region, and the right slab waveguide. In the second step, the calculated three effective indices will be taken as the refractive indices of the three layers in the second (vertical) planar waveguide. Then the overall propagation constants or effective index of the supported mode can be obtained by solving the planar waveguide eigenvalue equations again. Due to the polarization-dependent mode distribution, different solutions can be obtained for TE and TM modes. Here the eigenvalue equations are solved using EIM method in detail for TE mode only. Solutions for TM mode can be obtained in a similar way.

Consider the SOI rib waveguide as shown in Figure 2.2, the wave equation for TE mode is given by

$$\frac{\partial^2 H_x}{\partial x^2}+\frac{\partial^2 H_x}{\partial y^2}+\left[k^2 n^2(x,y)-\beta^2\right]H_x=0 \tag{2-2}$$

where $k=2\pi/\lambda$ is the wave number, $n(x,y)$ is the refractive-index of the SOI rib waveguide, and β is the propagation constant. In order to apply the effective index method, we can assume that the electromagnetic field can be expressed with the separation of variables as

$$H_x(x,y)=X(x)\times Y(y) \tag{2-3}$$

By substituting equation (2-3) into equation (2-2) and dividing by the product *XY* at both sides of the equation, we can obtain

$$\frac{1}{X}\frac{\partial^2 X}{\partial x^2}+\frac{1}{Y}\frac{\partial^2 Y}{\partial y^2}+\left[k^2 n^2(x,y)-\beta^2\right]=0 \tag{2-4}$$

Here we define an effective index distribution function $n_{eff}(x)$, which is a y-independent function. Then we can separate the equation (2-4) into two independent equations by adding and subtracting a y-independent term $k^2 n_{eff}^2(x,y)$ as

$$\frac{\partial^2 Y}{\partial y^2} + \left[k^2 n^2(x,y) - k^2 n_{eff}^2(x)\right] Y = 0 \tag{2-5a}$$

$$\frac{\partial^2 X}{\partial x^2} + \left[k^2 n_{eff}^2(x) - \beta^2\right] X = 0 \tag{2-5b}$$

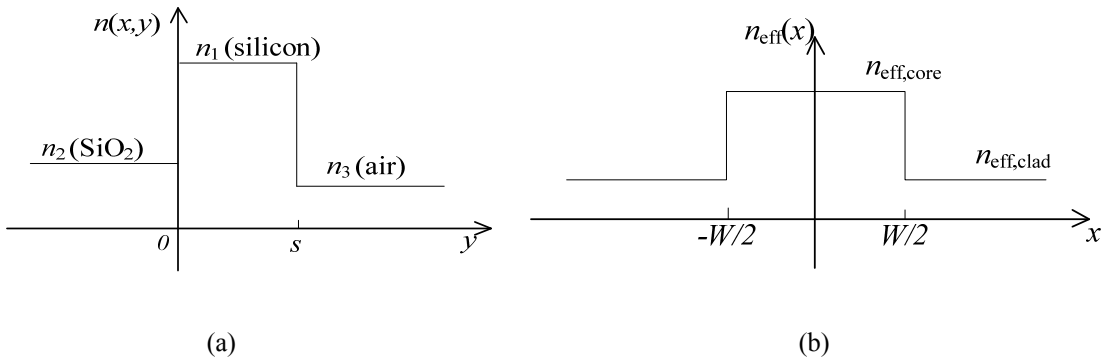

(a) (b)

Figure 2.3 Refractive index profiles in the effective index method. (a) Actual refractive index profile along y-direction; (b) Calculated effective index profile from the first step, forming a vertical planar waveguide.

The actual refractive-index profile $n(x,y)$ is plotted in Figure 2.3a, where s is the height of the rib. Depending on the position of x, s has the following two different values,

$$s = \begin{cases} H & |x| \le W/2 \\ T & |x| > W/2 \end{cases} \tag{2-6}$$

According to the effective index method, we first solve equation (2-5a) and determine the effective index profile $n_{eff}(x)$ along x-direction.

Along y-direction, the waveguide is asymmetric. We can define the following effective wavenumbers [31],

$$\begin{aligned} \kappa_y &= k\sqrt{n_1^2 - n_{eff}^2(x)} \\ \sigma_y &= k\sqrt{n_{eff}^2(x) - n_2^2} \\ \xi_y &= k\sqrt{n_{eff}^2(x) - n_3^2} \end{aligned} \tag{2-7}$$

Then the eigenvalue equation for the asymmetric waveguide for TE mode is given by

$$\kappa_y s = m\pi + \tan\frac{\sigma_y}{\kappa_y} + \tan\frac{\xi_y}{\kappa_y} \tag{2-8}$$

With the given values of the refractive indices and waveguide dimensions, equation (2-8) has a solution of κ_{y_core} for $m = 0$ order (fundamental mode) in the waveguide region of $|x| \le w/2$. Similarly, in the region of $|x| > w/2$, equation (2-8) has another solution of κ_{y_clad} for fundamental mode. Therefore, the effective index profile of the SOI waveguide is given by

$$n_{eff}(x) = n_{eff,core} = \sqrt{n_1^2 - \left(\frac{\kappa_{y\_core}}{k}\right)^2} \qquad |x| \le w/2 \tag{2-9a}$$

$$n_{eff}(x) = n_{eff,clad} = \sqrt{n_1^2 - \left(\frac{\kappa_{y\_clad}}{k}\right)^2} \qquad |x| > w/2 \tag{2-9b}$$

After the first step, EIM method creates a vertically symmetric planar waveguide with the refractive index distribution shown in Figure 2.3b.

Then in the second step, we need to solve the wave equation (2-5b) and determine the propagation constant β for TE mode. We can also define the following effective wavenumbers along *x*-direction,

$$\kappa_x = \sqrt{k^2 n_{eff,core}^2 - \beta^2}$$
$$\sigma_x = \xi_x = \sqrt{\beta^2 - k^2 n_{eff,clad}^2} \qquad (2\text{-}10)$$

In this case, the eigenvalue equation for the formed symmetric waveguide is given by $\kappa_x w = m\pi + 2\tan\frac{\sigma_x}{\kappa_x}$. For the fundamental mode ($m = 0$), a solution of κ_x can be obtained. Finally, the propagation constant and the effective index of the TE mode in the SOI rib waveguide is obtained as $\beta = \sqrt{k^2 n_1^2 - \kappa_x^2}$ and $n_{eff} = \frac{\beta}{k}$, respectively.

2.2.2. Finite Element Method (FEM)

In analysis of SOI waveguides, analytical methods, such as the above mentioned EIM method, are applicable only to waveguides with simple geometries and uniform material compositions, since their analytical models are defined over the entire waveguide region. To accurately analyze SOI waveguides with complicated cross-sectional structures and arbitrary refractive index profiles, some numerical analysis methods employing subdivision processes are developed.

The finite element method (FEM) is one of the most popular numerical methods with subdivision process [31]. In FEM method, the entire waveguide (model) region is divided into many discrete elements, which are usually in triangular shape. Mathematically, the FEM method can find approximate solutions of partial differential equations. The method assumes

the piecewise continuous function for the solution. In the case of analysis of the propagation properties of a two-dimensional SOI waveguide, the partial differential equations are derived from the wave equation over a large amount of discrete elements with appropriate boundary conditions. The solution of the wave equation in each element can be approximated by a linear function of the coordinates. The overall solution (the propagation constant and the electric field distribution) of the entire waveguide region is obtained by the summation of the individual element.

It is worth pointing out that the accuracy of the FEM solution is determined by the total number of the divided elements (mesh density). While simply increasing the number of elements can improve the accuracy of the solution, this may also cause a greatly increased computing time. To find a balance between the accuracy and the computing time, a convergence analysis is generally implemented to determine a proper mesh density required to obtain an acceptable accuracy.

2.2.3. Finite Difference Time Domain (FDTD) Method

The finite difference time domain (FDTD) method is another widely used computational modeling technique for electromagnetic field analysis in SOI waveguides. According to Maxwell's differential equations, the change in the electric field in time is determined by the change in the magnetic field across the space. In another word, at any specific point in space, the updated electric field in time is determined by the previously maintained electric field and the numerical curl of the local magnetic field in space. Similarly, the change in the magnetic field is time-stepped in the same way. The FDTD method finds solutions for Maxwell's equations by a proper discretization of both time and space domains using central-difference

approximations to the time and space partial derivatives. The resulting finite-difference equations can be solved in a leapfrog manner. The electric field vector components in a specific space are solved at a given instant time, and then the magnetic field vector components in the same spatial region are solved at the next instant time. Such a time-stepped process is implemented repeatedly until the entire electromagnetic field is fully solved.

The FDTD method is conceptually simple; the algorithm does not require the formulation of integral equation. It is simple to implement for complicated and inhomogeneous structures. Due to its time-domain nature, the frequency domain response over a wide range of frequencies can be easily obtained with a single simulation. However, since its implementation requires that the entire computational domain be gridded, and the grid discretization must be sufficiently fine to obtain both spectral resolution and spatial resolution, the required computing time may be very long.

2.2.4. Beam Propagation Method (BPM)

The beam propagation method (BPM) is another computational technique for simulating the propagation of light in slowly varying optical waveguides. With this method, the dynamic mode profile of an optical waveguide can be accurately estimated as the wave propagates through the waveguide. The BPM method essentially decomposes a supported mode into a superposition of plane waves, each traveling in a different direction. The individual plane waves propagate through a finite pre-determined distance in the waveguide until a certain point where the electromagnetic field is to be determined. At this specific point, all the arrived individual plane waves are numerically added together to reconstruct the spatial mode following the Fourier

theory. In BPM method, the fundamental idea is that a complicated problem (mode distribution in the waveguide) is decomposed into different simpler problems (different plane waves).

Like the above discussed FDTD method, the BPM method solves Maxell's equations by using finite differences in place of partial derivatives. However, as opposed to the FDTD method which is implemented in time domain, the BPM method is done entirely in the frequency domain. According to Fourier theory, any periodic signal can be decomposed into different frequency components (sinusoids). We can then reconstruct the original time domain signal by summating all of these sinusoids of different frequencies. Another key difference from the FDTD method is that in BPM, a slowly varying envelope approximation in the paraxial direction is required.

2.3. Coupling Light to Small SOI Waveguides

The compact dimension of SOI waveguides improves the packing density and performance of the silicon photonic integrated circuit. Since light emission is not easy to achieve in silicon and optical signal usually relies on the source from another chip through optical fiber connection, fiber-to-waveguide coupling is an important issue in practice. Due to the large difference between the dimensions of SOI waveguides and optical fibers, there is huge mismatch between the mode sizes of two waveguides, resulting in a big challenge in efficiently coupling light from optical fibers. For example, direct coupling light from optical fibers to small SOI waveguides results in coupling losses as high as 20 dB. Various methods have been proposed to achieve efficient light coupling from optical fibers to small SOI waveguides. The most commonly used coupling techniques include end-fire coupling, prism coupling, grating coupling and taper coupling. Each method will be described below in turn.

2.3.1. End-Fire Coupling

End-fire coupling is a very sample approach for coupling to/from small SOI waveguides, where the incident light beam from an optical fiber is shined onto the end of the SOI waveguide. To overcome the huge dimension difference between the two devices, end-fire coupling shrink the beam size by incorporating a lens to focus the input beam onto the endface of the waveguide, as shown Figure 2.4.

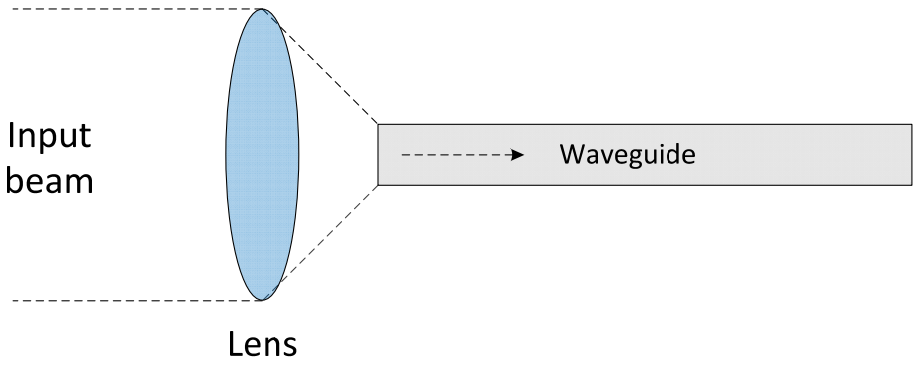

Figure 2.4 End-fire coupling.

In end-fire coupling, the coupling efficiency depends on the mode match between the transmitting waveguide and the receiving waveguide. Due to the use of focusing lens, the mode of the incident beam can be shrunk to match the mode that supported by the SOI waveguide, therefore end-fire coupling offers higher coupling efficiency than the direct butt-coupling approach. Mathematically, matching of the excitation modes can be evaluated by calculating the overlap integral between the excitation field and the waveguide field [37], where an assumption that the optical fiber and the SOI waveguide is perfectly aligned is made. In fact, alignment of those two devices is of critical importance due to the very small dimensions of the SOI waveguides. Even very small offsets between the two can cause significant losses. Spatial

misalignment of the excitation and waveguide fields should be considered when calculating the overlap integral.

In addition, the coupling efficiency of the end-fire approach is also dependent on the reflection from the waveguide facet. The reflection is caused by the refractive index mismatch between one medium (air) and another (SOI waveguide). Coupling losses caused by reflection from the waveguide endface can be analyzed using the Fresnel equations [37]. The quality of the waveguide endface also affects the coupling efficiency. To improve the overall coupling efficiency, the endface of the SOI waveguide should be carefully polished and coated with anti-reflection (AR) film. The numerical aperture is another parameter that can affect the coupling efficiency. It is usually required that the number aperture of the waveguide should be equal to or larger than that of the input field.

2.3.2. Prism Coupling

The prism coupler, as shown in Figure 2.5, couples the input light beam into a thin SOI waveguide through the top surface of the waveguide at a specific angle [51]. Therefore, the need for precision polishing of the endface of the waveguide and sub-micrometer accuracy in the alignment of the beam and the waveguide is avoided. By using a prism coupler, a large incident beam with a diameter hundreds of times the dimension of waveguide can be coupled into the waveguide.

To ensure high coupling efficiency (no light gets reflected from the bottom surface of the prism), a phase matching condition is to be satisfied between the propagation constant of the supported mode in the waveguide and the incident light at an angle normal from the waveguide surface,

$$\beta_p = \frac{2\pi}{\lambda_0} n_{SOI} \cos\theta \qquad (2\text{-}11)$$

where β_p is the propagation constant of the supported mode in the waveguide, λ_0 is the wavelength of the input light in vacuum, n_{SOI} is the refractive index of the SOI waveguide, and θ is the incident angle.

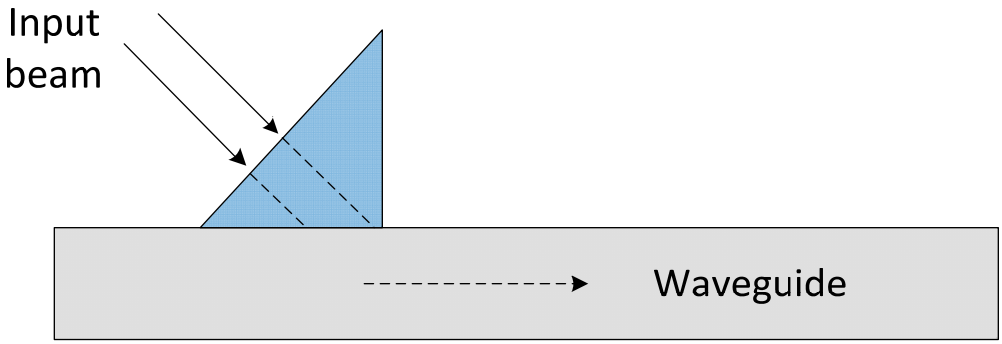

Figure 2.5 Prism coupling

Note that while prism coupling method works well for coupling light into thin films, it is not practically useful for SOI waveguides. The phase matching condition requires that the prism should have a higher refractive index than the waveguide. This requirement limits its practical applications since silicon has a very high refractive index of 3.5.

2.3.3. Grating Coupling

Similar to prism couplers, grating couplers also enable coupling of light into a SOI waveguide from the top surface of the waveguide [52]. Consequently, a phase matching condition like equation (2-11) should also be satisfied. As shown in Figure 2.6, a grating structure with periodic refractive index modulation is introduced on the top surface of the SOI waveguide. The

grating is properly designed such that only the -1 order diffracted light can satisfy the phase condition $\beta_p = \beta_W - \frac{2\pi}{\Lambda}$, where β_W is the propagation constant when the grating is not present and Λ is the grating period. Considering the propagation constant β_W can be expressed in terms of the effective index n_{eff} as $\beta_W = \frac{2\pi}{\lambda_0} n_{eff}$, the grating period that satisfies the phase matching condition for given wavelength and incident angle can be determined by

$$\Lambda = \frac{\lambda_0}{n_{eff} - n_0 \cos\theta} \tag{2-12}$$

where n_0 is the refractive index of the medium on top of the SOI waveguide. Equation (2-12) can then be used to determine the waveguide grating period for a desired incident angle for coupling to the mode with a propagation constant of β_W. Phase matching condition (2-12) only determines the grating period.

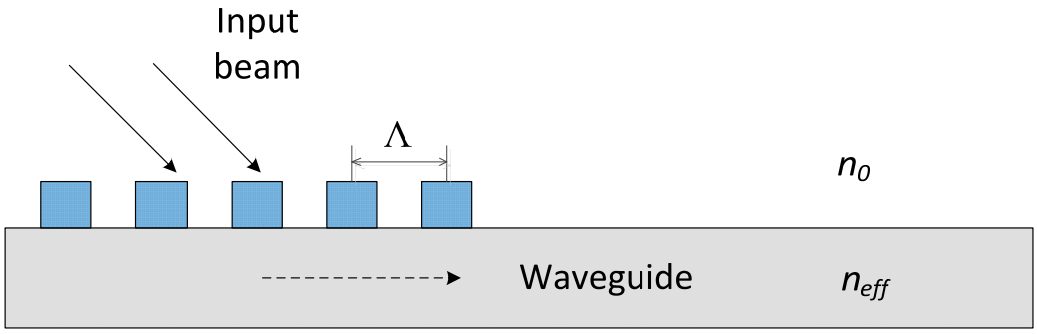

Figure 2.6 Grating coupling

It is worth noting that since the refractive index of silicon waveguide is large, the required period of grating in silicon for light coupling is very small (in the order of 400 nm for

telecommunication wavelength of 1550 nm). This strict requirement dramatically increases the fabrication difficulties. With the state-of-the-art waveguide fabrication technique, grating couplers with coupling efficiency as high as 80% has been demonstrated [53].

The conventional one-dimensional grating coupler only works for input light beam with single polarization (for example, TE-polarization). By using a two-dimensional (2D) grating coupler, the incoming light with an unknown polarization state can be coupled to the TE-polarization modes of the two planar waveguides [54]. By using this coupling scheme, the polarization dependence problem of coupling light to SOI waveguides can be solved.

2.3.4. Taper Coupling

Taper coupling can be incorporated with any above described coupling approach to further increase the coupling efficiency. A taper structure offers a gradual transition from a large cross-sectional waveguide area to a smaller one which is compatible to the small waveguide. The key issue in taper coupling is that a taper should reduce the waveguide dimensions in a smooth and lossless transition, which means that the angle of the taper should be very small for the smooth transition and the surface should have a very low roughness to reduce the scattering loss.

Tapered couplers usually can offer higher coupling efficiency than the grating coupler. Most of the couplers have linear tapers, while a few have exponential or parabolic tapers. The tapered couplers can be generally classified into two main categories: inverse tapers and standard tapers. The former increases from a very small point at the fiber end to the waveguide end and the latter decrease from a large dimension at the fiber end to a small dimension at the waveguide end. More complicated tapered couplers employ combinations of the two structures.

2.4. Propagation Loss Measurement in SOI Waveguides

When a SOI waveguide device is introduced into a system, extra losses would be also caused compared to the system when the device is not inserted. The insertion loss of a waveguide or device is the total loss and includes both the inherent loss of the waveguide itself when light is propagation through it and the coupling losses when the waveguide is shined with the input light beam. Coupling loss of SOI waveguides has been discussed in 2.3. Here the propagation loss when the light is travelling in the waveguides is described and the techniques for measuring propagation loss in SOI waveguides are presented.

2.4.1. Sources of Propagation Loss in SOI Waveguides

There are three main sources that contribute to the propagation loss in SOI waveguides: scattering loss, absorption loss and radiation loss.

Scattering loss is usually caused by the imperfections in the waveguide material (known as volume scattering) or the roughness at the interface between the core and claddings (known as surface scattering). While silicon waveguides are usually low loss, SOI waveguides may have some defects introduced during the fabrication process, such as ion implantation. Those defects in the SOI waveguides cause non-negligible volume scattering loss. It is obvious that volume scattering loss depends on the number of defects, the size of defects with respect to the wavelength of propagation, and the correlation length along the waveguide.

Absorption loss in silicon waveguides are usually caused by interband absorption and free carrier absorption. When photons with energy larger than the band gap of the waveguide material propagate through the waveguide, interband absorption occurs such that the photons

are absorbed and electrons are excited from the valence band to the conduction band. To efficiently avoid interband absorption, a wavelength must be longer than the absorption edge wavelength of the waveguide material. The band edge wavelength of silicon is about 1.1 um, making it a perfect low-loss waveguide for telecommunication wavelength at 1550 nm band. While the interband loss in silicon waveguide is low, free carrier absorption may affect dramatically the propagation loss in silicon waveguide. The concentration of free carriers can change both the real and imaginary refractive indices. The former can be used to achieve high-speed modulation in silicon and the latter contributes to the absorption loss in the silicon waveguide.

Radiation loss is usually caused by the leakage from the waveguide into the surrounding media. For a strip waveguide, leakage occurs from the waveguide core layer to the upper or lower cladding layers. For a rib waveguide, light may be leaked into the planar area adjacent to the core region. In the case of SOI, the buried silicon dioxide layer must be sufficiently thick to prevent the confined optical modes from penetrating the oxide cladding layer and coupling to the silicon substrate. For straight silicon waveguides with tight light confinement, radiation loss is negligible. However, for curved waveguides, radiation loss is a big issue as the curvature of the waveguide will change the angle of incidence at the waveguide side wall, resulting in serious radiative loss. The loss coefficient is critically dependent upon the radius of curvature of the bending waveguide. Consequently the radius of curvature must be as large as possible to minimize radiation loss. However, for most applications a small device footprint is desirable, implying that the radius should be as small as possible. Therefore, new type of SOI waveguide devices that can turn the light propagation direction are developed, such as the corner turning mirror, which will be discussed in details in Chapter 3.

2.4.2. Measurement of Propagation Loss in SOI Waveguides

This thesis is about the performance characterization of the passive SOI waveguide devices. Propagation loss is a key parameter to be characterized. Here several techniques for waveguide propagation loss measurement are described, including the cut-back method, the Fabry-Perot resonance method, and scattered light measurement method.

The cut-back Method

As the simplest method of measuring propagation loss of an optical waveguide, the cut-back method has been widely used for SOI waveguides. The cut-back method is usually associated with either end-fire coupling. Its basic idea is that propagation loss of a SOI waveguide can be unambiguously determined by measuring two waveguides with different length, such that the coupling loss of the waveguide can be eliminated from the measurement. Considering the same input optical power is shined, by the same coupling condition, into two waveguides with lengths of L_1 and L_2, output optical powers of I_1 and I_2 are obtained. Then the propagation loss of the same waveguide with the length of $L_1 - L_2$ can be calculated from the difference in the output power from each measurement. We define the loss coefficient α as a measurement that how the intensity decays with propagation distance *z* through a waveguide,

$$I_{out} = I_{in} \exp(-\alpha z) \tag{2-13}$$

Then the propagation loss coefficient can be determined as

$$\alpha = \left(\frac{1}{L_1 - L_2} \right) \ln(I_2 / I_1) \tag{2-14}$$

Note that to maintain good accuracy in the cut-back method, the input coupling, the condition of the waveguide endfaces, and the input power should all remain constant.

The Fabry-Perot Resonance Method

The cut-back method is destructive to the waveguide to be measured and requires multiple measurements. Therefore its applications in practice are limited. The Fabry-Perot resonance method enables more accurate and single-time measurement for propagation loss in silicon waveguides.

When light propagates along the waveguide, due to the reflection at either endface, the waveguide can form a resonant cavity, so-called Fabry-Perot cavity. The optical intensity transmitted through the cavity is related to the facet reflectivity, the waveguide length and the propagation loss coefficient. Therefore, by measuring the waveguide length and the minimum and maximum transmitted optical power, the loss coefficient can be determined. One feature of the Fabry-Perot resonance method is that the coupling efficiency does not affect the calculation of the loss coefficient. This method can be particularly useful for measuring low-loss SOI waveguides with high accuracy. In this thesis, the propagation loss of the SOI waveguides is measured using Fabry-Perot resonance method. More details will be discussed in Chapter 3.

Scattered Light Measurement

The propagation loss in a SOI waveguide can also be evaluated from the measurement of scatted light from the surface of the waveguide. Since the amount of the scattered light is proportional to the propagating light, if the scattered light is measured as a function of waveguide length, the decay rate of the propagating light and hence the loss coefficient can be

determined. To measure the scattered light, an optical fiber can be scanned along the surface to collect the scattered light. Note that if the loss of the SOI waveguide is low, the scattered light will be too weak to be detected. Therefore this method works only if the loss of the waveguide is high and relatively high optical power is propagating in the waveguide. These requirements limit its utility in practical applications. The scatter light measurement is usually used for initial studies of high-loss waveguide materials.

CHAPTER 3 SOI RIB WAVEGUIDE BEND AND CORNER DEVICES

As micro electronic manufacturing technology is becoming more mature, SOI waveguides have been extensively applied as a new platform of photonic integrated circuits (PIC). To maximize the intensity of PIC components on a single SOI chip, the compact and low loss SOI waveguide bends or corners are required. In this Chapter, a new SOI rib waveguide corner device, corner turning mirror, is studied. The corner turning mirrors allow compact 90^{o} turns between two perpendicular waveguides. Its performance is characterized and compared to that of the conventional SOI rib curved waveguides.

3.1. Introduction

Silicon-on-insulator (SOI) waveguide has found numerous applications within the field of photonic integrated circuits (PIC) [2]. The key features of SOI technology include its compact confinement due to the high refractive index contrast of SOI waveguides between silicon layer and silicon dioxide substrate and good compatibility with the modern micro-electronics, such as complementary metal-oxide semiconductor technologies. Thanks to the strong light confinement, an SOI strip waveguide can tightly confine light to sub-wavelength cross-sections (a few hundred nanometers) while still satisfying the single-mode transmission operation. More compact footprint of the integrated photonic device is hence made possible. The development of such photonic nanowires inspires the intense investigation in photonic processing chips and systems. However, such small dimensions create difficulties in fabrication process and suffer

from the high coupling losses at interfaces between waveguides and fibers and active and passive devices on one single chip [55]. On the other hand, the SOI rib waveguides are attractive because they support single mode transmission at larger scales (a few micrometers) and hence easy to fabricate.

In PIC-based systems, more and more components with different functionalities are to be integrated on a single SOI chip. To increase the integration density of an SOI chip, low-loss compact SOI waveguide bend or corner structures are in high demand. Unfortunately, a conventional SOI rib waveguide bend does not fulfill this requirement, since the minimum acceptable radius curvature of the rib waveguide bend structure is quite large due to the lower optical confinement associated with the relatively small refractive index contrast of SOI rib waveguides in the lateral direction than a SOI strip waveguide [56]. For rib waveguides, circular bends must have a radius curvature larger than tens of micrometers to reduce the radiation loss to an acceptable level.

As a promising solution, SOI waveguide corner-mirror structures based on total internal reflection have been a research topic of increasing interest [57-59]. SOI curved waveguides and corner turning mirror (CTM) structures with different parameters have been designed and fabricated based on the theoretical model. In this chapter, the performance comparison between the SOI curved waveguides and the CTM structures, such as the propagation loss and polarization dependent loss, is presented. A complete SOI chip testing setup has been built. The optical propagation loss and polarization dependent loss of the two different SOI structures have been measured using an optical vector analyzer (LUNA technology). The testing results show that the innovative SOI CTM structures can not only significantly reduced the footprint size of

the SOI chip, but also improve both the insertion loss and polarization dependent loss by replacing the curved sections in any SOI planar lightwave circuit systems.

3.2. Propagation Loss Measurement of SOI Curved Waveguides

The accurate performance measurement of SOI-waveguides is significantly important in integrated optics. The optical loss is an elementary evaluation for a SOI waveguide device. As described in Chapter 2, many direct measurement techniques have been available for waveguide propagation loss measurement, such as waveguide scattered light measurement [60] and waveguide transmission measurement [61]. The accuracy of these methods either depends strongly on the quality of the waveguide surface or is significantly affected by the unstable measurement of the fiber-waveguide coupling loss. A simple cut-back method has been developed to mitigate these problems [62]. However, multiple sample lengths have to be measured for the same waveguide device and keeping exactly the same coupling efficiency for different samples over different measurements is a big challenge. Recently, an accurate waveguide propagation loss measurement method based on Fabry-Perot interference principle has been proposed [60, 63, 64]. The propagation loss is extracted from the Fabry-Perot resonance fringes without the consideration of fiber-waveguide coupling efficiency. The Fabry-Perot interferometric method has been widely applied in propagation loss measurement for straight single-mode and multimode semiconductor waveguide.

In this thesis, the Fabry-Perot interferometric method is investigated to develop a general function for measuring both the propagation and bending/radiation losses of single-mode SOI curved waveguides, which are key components of determining the integration density of planar lightwave circuits on a single SOI rib waveguide chip. The developed, generalized Fabry-Perot

interferometric method is assisted by Luna-system, which is an optical vector-matrix analyzing technique used to measure the broadband Fabry-Perot spectral resonance fringes. The combination of the generalized Fabry-Perot interferometric method and the Luna testing technology can accurately and unambiguously measure the propagation loss of different SOI waveguide devices.

3.2.1. Fabry-Perot Interferometric Method

A generalized analyzing model based on Fabry-Perot interferometric method is proposed to measure the propagation loss and bending/radiation loss of SOI curved waveguides. An SOI optical waveguide with polished end facets is structurally similar to the Fabry-Perot cavity of a laser. For a fiber-DUT-fiber measurement system, where DUT stands for the photonic integrated device under testing, the two facets of the DUT form a Fabry-Perot cavity, as shown in Figure 3.1.

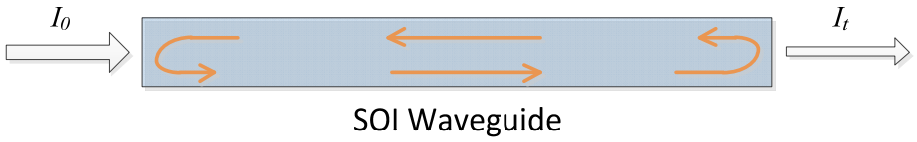

Figure 3.1 Fabry-Perot cavity formed by two end facets of a SOI waveguide.

If the incident light is normal to the facets, the optical intensity transmission function through the Fabry-Perot cavity showing the relationship between the transmitted and the incident light is given by [63],

$$T_g = \frac{I_t}{I_0} = \frac{(1-R)^2 A_g}{(1-A_g R)^2 + 4A_g R \sin^2(\delta/2)} \tag{3-1}$$

where R is the facet reflectivity, which is typically determined from effective index measurements of the surrounding medium (such as air) and waveguide as

$$R = \left| n_{eff} - n_{air} \right|^2 \Big/ \left| n_{eff} + n_{air} \right|^2 \tag{3-2}$$

A_g is the general attenuation coefficient and $\delta = 4\pi n_{eff} L/\lambda$ is the phase change of a round beam travel in the Fabry-Perot cavity, n_{eff} is the effective index of the waveguide, and L is the total waveguide length (physical cavity length). Since this phase term is wavelength-dependent, the optical intensity transmission function (3-1) has a nearly sinusoidal resonance fringe, as shown in Figure 3. 2.

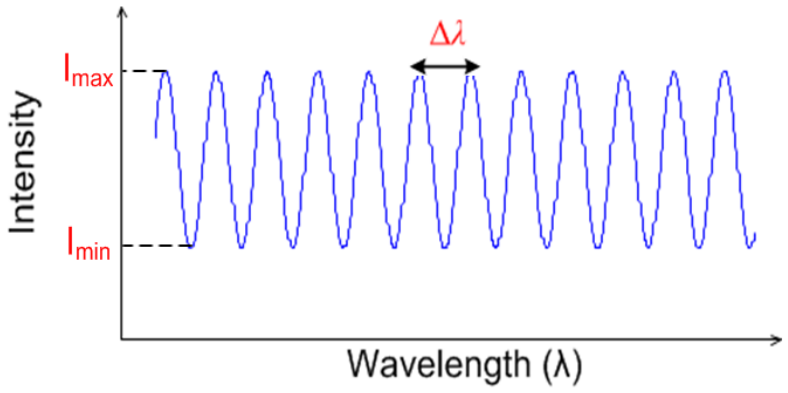

Figure 3.2 Illustration of optical intensity transmission function of the Fabry-Perot cavity according to equation (3-1).

At certain wavelengths, the round trip phase term satisfies that $\delta = 2m\pi$, which will lead to a maximum intensity transmission of

$$T_{g\max} = \frac{I_{t\max}}{I_0} = (1-R)^2 A_g \big/ (1 - A_g R)^2 \tag{3-3a}$$

While at other wavelengths, the phase term reaches $\delta = (2m+1)\pi$, which will result in a minimum transmission of

$$T_{g\min} = \frac{I_{t\min}}{I_0} = (1-R)^2 A_g \Big/ (1+A_g R)^2 \tag{3-3b}$$

Therefore, by measuring the maximum and minimum value of the intensity transmission function (or equivalently the transmitted optical power for a given initial input power) over a broad spectral range, the general attenuation coefficient A_g can be accurately and unambiguously determined as

$$A_g = \frac{1}{R} \times \frac{\sqrt{I_{t\max}/I_{t\min}} - 1}{\sqrt{I_{t\max}/I_{t\min}} + 1} \tag{3-4}$$

Given that there are *N* elements and/or structures that can individually cause attenuations to an optical beam, a general attenuation coefficient can then be expressed as

$$A_g = \prod_{j=1}^{N} A_j \tag{3-5}$$

where A_j is the attenuation coefficient of the *j*'th element or structure. Considering a straight SOI waveguide guide, for example, the general attenuation coefficient can be expressed as $A_g = \exp(-\alpha_{prop} \cdot L_{WG})$, where α_{prop} is the propagation loss rate and L_{WG} is the total length of the waveguide. Then the propagation loss coefficient α_{prop} (dB/cm) can be calculated as

$$\alpha_{prop} = -\ln\left(A_g\right) \Big/ L_{WG} \tag{3-6}$$

According to the above described Fabry-Perot interferometric model, the total length of a SOI waveguide device can be determined from the free spectral range (FSR) of the Fabry-Perot resonance fringe as

$$L_{WG} \approx \frac{\lambda^2}{2n_{eff}\Delta\lambda} \tag{3-7}$$

where $\Delta\lambda$ is the FSR of the spectral resonance fringe, as shown in Figure 3.2. Therefore, the total propagation loss and the waveguide length of a SOI waveguide device can be obtained from a single measurement of the Fabry-Perot resonance fringes, according to (3-4) and (3-7). Note that in order to measure the pure bending/radiation loss of a SOI curved waveguide, the propagation loss coefficient of a SOI straight waveguide should be first determined.

3.2.2. Measurement System

The general model described in the previous section works for optical propagation loss measurement of many other photonic integrated devices. In this Chapter, we use it to measure propagation loss of single-mode SOI curved waveguides. Figure 3.3(a) shows the experimental setup to measure the loss of the SOI waveguide device under test (DUT). Two high-precision x-y-z axis stages are used to hold the input and output fiber tips for optical coupling. An optical vector analyzer (Luna system) is used to measure device length and the broadband spectral response of the SOI devices under test. A polarization controller is used, so that we can measure the polarization-dependent propagation loss of the SOI chip. Fig. 4(b) shows the picture of the test bed. A piezoelectric transducer (PZT) controlled precise three-dimensional moving stage is used to perform the accurate optical alignment between the fiber tip and SOI chip. The coupling technique is end-fire coupling. Lensed fibers are used to increase the coupling efficiency.

Coupling efficiency of 50% is estimated. Optical power from the output facet of the device is collected using another lensed fiber and sent back to the optical vector analyzer. Fabry-Perot resonance can be measured and the propagation loss can be calculated.

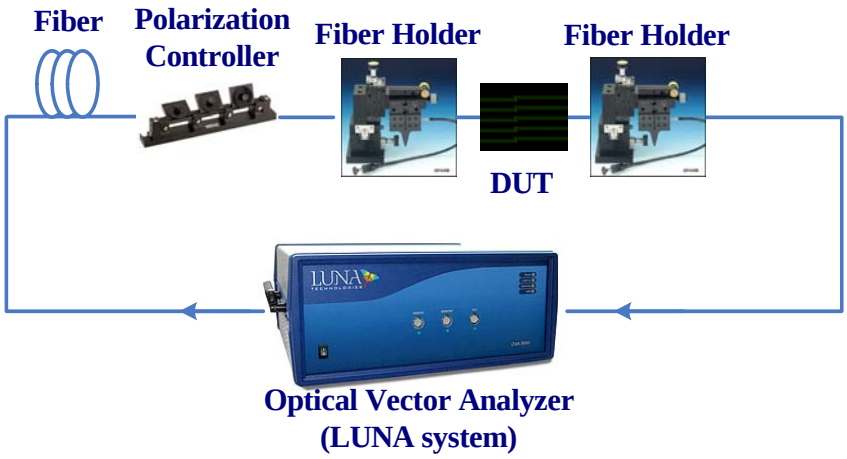

(a)

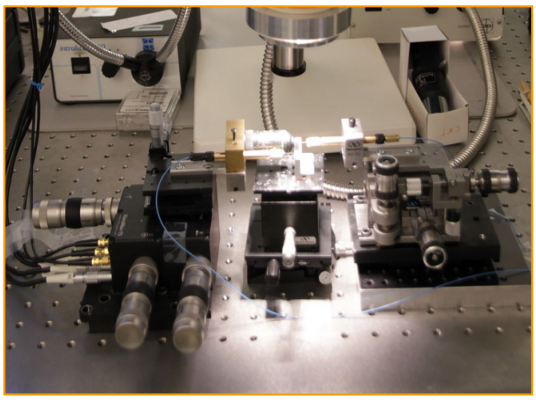

(b)

Figure 3.3 Experimental setup for measurement of propagation loss in SOI curved waveguides. (a) The measurement setup, and (b) a photo-picture of test-bed.

Note that in the Fabry-Perot interferometric method, it is assumed that the input optical power does not change during the measurement of Fabry-Perot fringes. This assumption is usually not satisfied. For example, if a tunable laser is used, the wavelength is scanned to cover the large spectral bandwidth. It is difficult to always keep the input power constant due to the stability of the laser of due to the change of coupling efficiency during the scan. If a broadband low-

coherence optical source (such as an amplified spontaneous emission source) is used, the optical power inherent changes with different wavelengths. One solution is to use a modified Fabry-Perot interferometric method [63]. However, complicated data processing is required. Another solution is to directly measure the spectral response of the device under test, such that the variation of the input optical power can be automatically compensated. In this thesis, the device response is measured using an optical vector analyzer in a very fast manner. Coupling condition can be easily maintained during the quick measurement.

3.2.3. Optical Vector Analyzer

In this thesis, an optical vector analyzer (OVA) form LUNA technology is employed to accurately measure the waveguide length and power ratio between input and output signals. The optical vector analyzer is operating based on swept wavelength interferometry (SWI) [65] or equivalently optical frequency domain reflectometry (OFDR) [66]. In an optical vector analyzer, a tunable laser source is used in associated with two concatenated Mach-Zehnder interferometers. The laser source has a narrow line-width of 200 kHz, and can be fast tuned at 70 nm/s.

The optical vector analyzer interrogates the optical device or system under test using swept-wavelength coherent interferometry by measuring the Jones matrix of the DUT. It is well known that the Jones matrix contains all of the information that is required to characterize the complete component performance, such as loss, dispersion, polarization effects, etc. The full scalar response such as both phase and amplitude information can be extracted from the Jones matrix in an accurate and fast manner in the form of polarization-averaged group delay, polarization mode dispersion, insertion loss, and polarization dependent loss.

The measured data can be presented for both the time domain and the frequency domain. The amplitude of the time domain data is equivalent to a traditional optical time domain reflectometry (OTDR) measurement. The amplitude of the frequency domain data provides a direct measure of the insertion loss or return loss of the device over a broad spectral bandwidth. The phase information in the frequency domain could be used to obtain group delay and chromatic dispersion.

Due to the interferometry nature of the optical vector analyzer, the OFDR measuring optical paths is up to 35 m long in reflection and 70 m in transmission without any dead zones (our experimental path is less than 5 m here). It can also measure group delay changes up to 350 ns, provides 80 dB of dynamic range and 100 dB sensitivity, and resolves individual features with spatial resolution down to 20 um. These features make the optical vector analyzer a powerful instrument for high resolution metrology of passive optical components.

3.2.4. SOI Curved Waveguides

The insertion loss, propagation loss and bending/radiation loss of SOI curved waveguides are measured in this thesis. As discussed above, low-loss and compact SOI curved waveguides are essential in photonic integrated circuits to increase the integration density of an SOI chip. However, there is a limit on the minimum acceptable radius curvature of the SOI rib waveguide bend structure due to the lower optical confinement associated with the relatively small refractive index contrast of SOI rib waveguides in the lateral direction. Therefore, it is necessary to accurately measure the propagation loss and bending loss of the SOI curved waveguides.

We have designed SOI curved waveguides with different rib sizes and radius curvatures. We fabricated the SOI devices in Canadian Photonics Fabrication Centre (CPFC) with a fabrication

grant from Canadian Microsystems Corporation (CMC). The manufacturing technology for the designed SOI curved waveguides is high-precision electron-beam lithographic fabrication with non-contact mask operations.

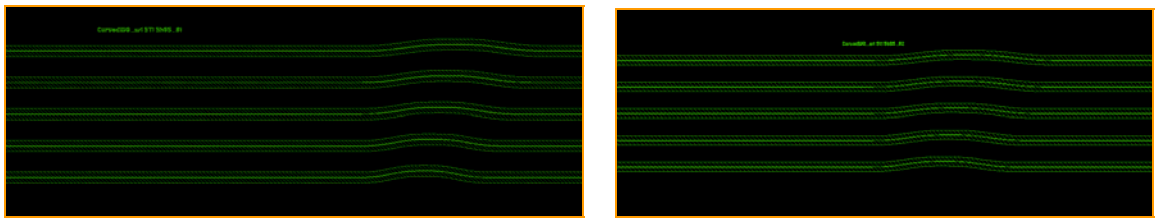

Figure 3.4 Micro-photo images of the SOI curved waveguides with different rib sizes and radius curvatures fabricated in CPFC.

Figure 3.4 shows the micro-photo images of the fabricated SOI curved waveguides with different rib sizes and radius curvatures, which are the samples used for measuring propagation and bending/radiation losses in our experiments. The fabrication quality is evaluated through measurements of the feature values in waveguide dimensions. Note that for the deep trench, the dimension error is 0.23μm within a 10.0μm dimension and the sidewall angle error is 0.6° in a 1.5μm depth.

3.2.5. Measurement Results

In this section, the insertion losses of single-mode SOI curved waveguides are first measured using the cut-back measurement method as discussed in Chapter 2 with the help of the optical vector analyzer. Two groups of reference waveguides with the same physical parameters with the waveguides under test but only different waveguide lengths are first tested. Then two groups of SOI curved waveguides under test with rib sizes of 3.5 and 4.0 μm are tested. Figure 3.5(a) shows the zoom-in view of the first group of five curved waveguides. Each group of

waveguides has different radius curvatures ranging from 0.5 mm to 1.05 mm. The device length of the SOI curve waveguide is measured to be 4.0 mm. The curve radius values of five curved waveguides in each group are 1.056, 0.9, 0.756, 0.625 and 0.506 mm. Here only TE-mode is tested, Figure 3.5(b) shows the mode field of the waveguide, which is detected by an infrared camera. The measured mode field verifies the single-mode operation of the SOI rib waveguides.

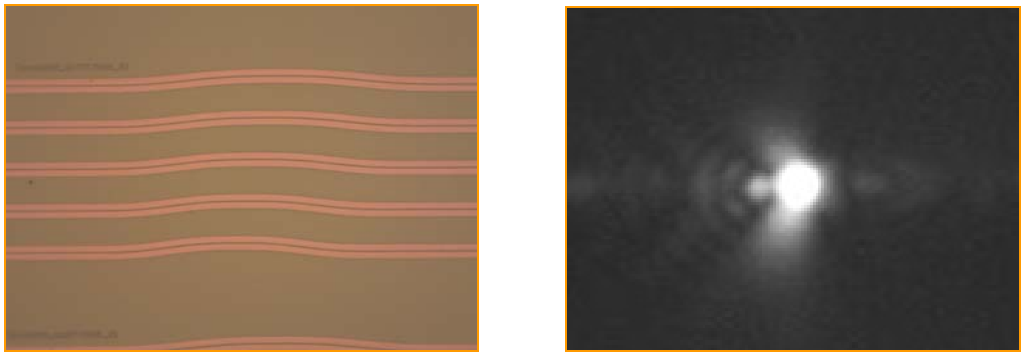

(a) (b)

Figure 3.5 (a) First group of SOI curved waveguides under test with rib size of 3.5 um. (b) Measured far-field mode pattern using an infrared camera, verifying single-mode operation of the SOI rib waveguides.

The insertion loss of two groups of SOI curved waveguides is measured using the testing setup shown in Figure 3.3(a). The optical vector analyzer is used to measure data in frequency domain. Figure 3.6(a) and (b) show the measured insertion loss of two groups of curved SOI waveguides over a broad spectral range. From Figure 3.6 we can find that with a given rib waveguide size, larger curve radius introduces smaller insertion loss and with a given curve radius value, larger rib waveguide size brings larger propagation loss. The measured results match well with the theoretical predictions.

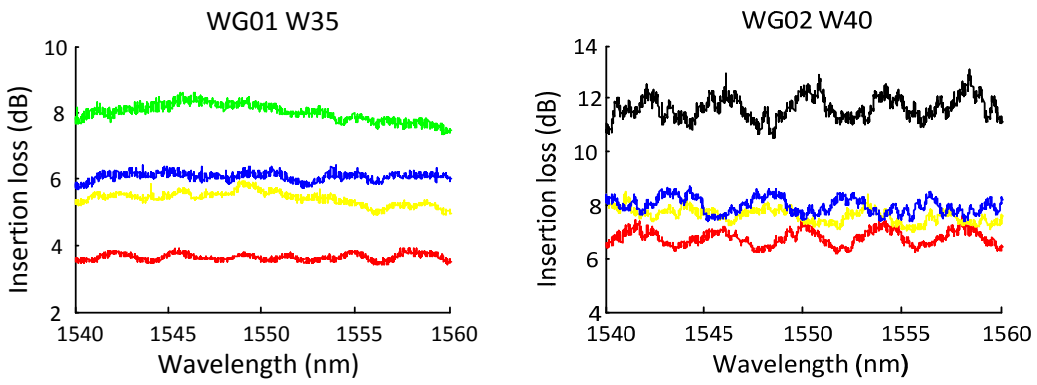

(a) (b)

Figure 3.6 Measurement results of the SOI curved waveguides (TE-mode only). (a) Insertion loss of the first group of SOI curved waveguides under test with rib size of 3.5 um and different radius curvatures. (b) Insertion loss of the second group of SOI curved waveguides under test with rib size of 4.0 um and different radius curvatures.

The cut-back method only provides insertion loss information of the waveguide. Here, the propagation loss and bending/radiation loss of SOI curved waveguides are measured using the Fabry-Perot interferometric method. To separate the propagation loss and bending loss of an SOI curved waveguide, the propagation loss of an SOI straight waveguide with the same rib size (3.5μm) as the curved waveguide is first measured using the Fabry-Perot interferometric method, which is estimated to be α_{stra} = 1.3dB/cm.

Then the optical bending/radiation loss of an SOI curved waveguide (as shown in Figure 3.5(a)) with the same rib size as the straight waveguide and 1806 μm radius is analyzed using the proposed Fabry-Perot interference method with the help of the optical vector analyzer (Luna system). The broad band spectrum of Fabry-Perot resonance fringes (the spectral response of the SOI curved waveguide) is measured using the Luna System, with the result shown in Figure 3.7. Since the free spectral range (FSR) of the fringes is $\Delta\lambda$ = 0.072 nm, the total waveguide length is determined to be L_{WG} = 4.8 mm according to equation (3-7). The maximum and the

minimum of the intensity transmittance curve are 0.615 and 0.39, respectively. Then based on the Fabry-Perot resonance method, the total propagation loss of the curved waveguide is estimated to be 4.27 dB according to equation (3-6).

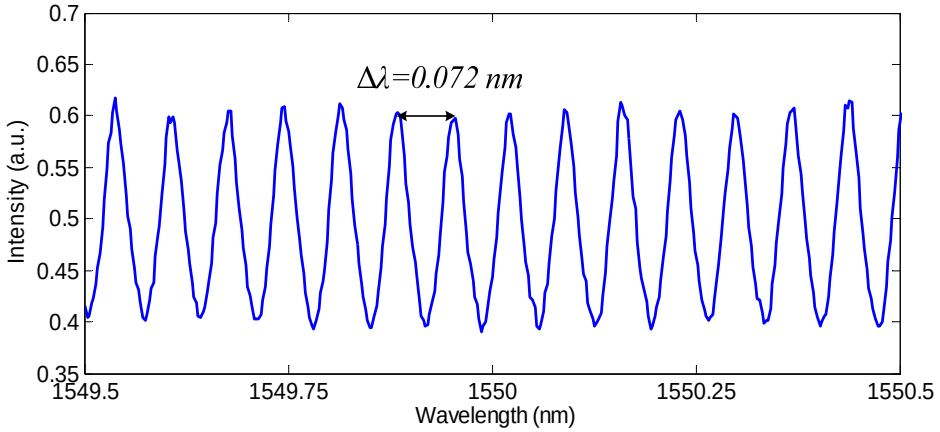

Figure 3.7 The measured broadband Fabry-Perot interferometric fringe of the SOI waveguide under test.

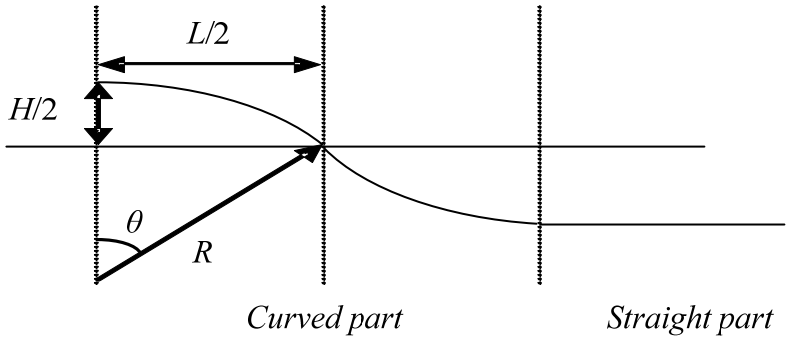

Figure 3.8 The half bend part of the curved SOI waveguide.

The total propagation loss consists of two parts: 1) pure propagation loss in the whole SOI waveguide without considering any radiation, and 2) the bending loss in the curved part. The former can be easily determined given that the total waveguide length L_{WG} and the propagation loss coefficient α in the straight waveguide have been determined. The latter can be obtained

by subtracting the propagation loss from the total loss. The waveguide length of the bending part, L_{bend}, can be calculated from the curved waveguide structure as shown in Figure 3.8.

$$L_{bend} = 4R\theta \cong 8Rtg^{-1}\left(\frac{H}{L}\right) \tag{3-8}$$

Finally, the optical bending loss coefficient of the curved SOI waveguide is estimated as

$$\alpha_{bend} = \frac{4.27 - \alpha_{stra} L_{WG}}{L_{bend}} = 2.142\ dB/mm \tag{3-8}$$

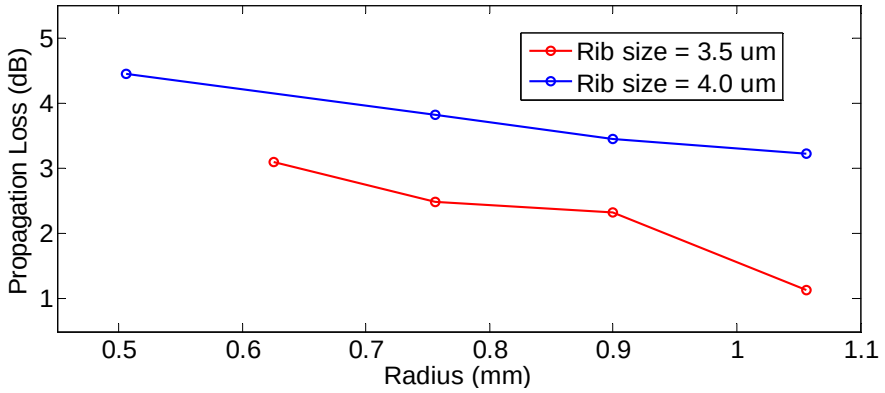

Figure 3.9 Measured propagation loss of two groups of SOI curved waveguides with different rib sizes and curve radius.

Total insertion loss of the two groups of SOI curved waveguides with rib sizes of 3.5 and 4.0 μm have been tested using the cut-back method. Here using the Fabry-Perot interferometric method, the propagation loss of the two groups of SOI curved waveguides are then tested. Figure 3.9 summarizes the measurement results at central wavelength of 1550 nm. We observe that with a given rib waveguide size, larger curve radius brings smaller propagation loss and with a given curve radius value, larger rib waveguide size results in larger propagation loss. Same results have been obtained by both two measurement methods.

3.2.6. Discussion and Summary

In this demonstration, only SOI curved waveguide is analyzed. In fact, Fabry-Perot interferometric method provides an efficient solution to measure all the loss sources of an SOI waveguide device. For example, to measure the access loss of a SOI corner-turning-mirror structure, the propagation loss of a straight waveguide must be determined first. Then the access loss of corning-turning mirror can be calculated according to equation (3-4).

In summary, the propagation loss and bending loss of an SOI curved waveguide were analyzed using a generalized Fabry-Perot interference method assisted by an optical vector analyzer (Luna system). The combination of Fabry-Perot resonance method and Luna System provides an efficient and accurate solution for measuring all the loss sources of an SOI waveguide device.

3.3. Loss Measurement of SOI Corner Turning Mirrors

As discussed above, to maximize the integrity of photonic integrated components on a single SOI chip, the compact and low loss SOI waveguide corners are required. In the past decade, there are numerous theoretical analyses for the rib waveguides corners [67, 68]. However, few works have been reported so far on the design and fabrication of the reflector [57, 58], though it has a great impact on the performance and the integration of devices and/or components. In fact, an adoptable structure of corner mirrors is a dominant element in building the complicated multiple-function photonic circuits.

Most recently, a comprehensive theoretical model and systematic discussion on the design and optimization of the reflector for SOI waveguide corner structures have been reported by our group [69]. The combined effect of the most significant physical factors is taken into account.

SOI corner turning mirror (CTM) structures with different parameters have been designed and fabricated based on the theoretical model. In this section, the performance of the SOI CTM devices are measured and compared to that of the SOI curved waveguides. The testing results show that the innovative SOI CTM structures can not only significantly reduced the footprint size of the SOI chip, but also improve both the propagation loss and polarization dependent loss by replacing the curved sections in any SOI planar lightwave circuit systems.

3.3.1. SOI Corner Turning Mirrors (CTM)

SOI CTM structures are based on optical total internal reflection (TIR) principle [57, 58]. Therefore a sharp (90 degree) turning angle can be achieved. Figure 3.10 shows the standard geometry (top view) of a SOI rib waveguide-based corner turning mirror structure, which is composed of waveguides and reflection mirror. L_m and W_m are the length and width of the reflector part, respectively. To ensure high reflectivity, the reflection mirror is usual made of air. Strong reflection is caused due to the significant refractive index different between the silicon waveguide and the air.

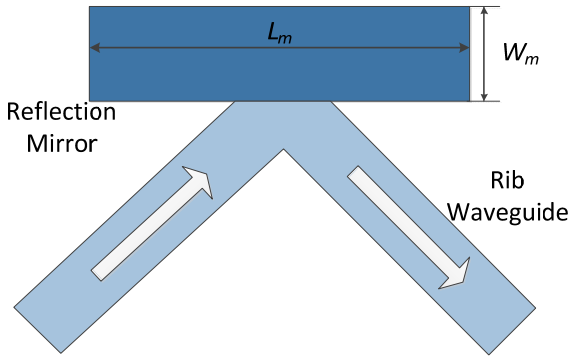

Figure 3.10 standard geometry of a SOI rib waveguide based CTM structure. *L* and *W* are the length and width of the CTM reflector, respectively.

Figure 3.11(a) show a cross-section view of the SOI rib waveguide that is used to form a corner turning mirror structure. *T* and *h* are the width and height of the SOI rib, respectively, and *H* is the total thickness of the silicon layer of the SOI waveguide structure. These waveguide parameters should be carefully designed to maintain single-mode condition [49, 50]. In addition, the mode size, which is directly determined by the waveguide parameters, is another very important factor in determine the mirror size. It has been reported that a smaller mode size has lower reflection loss at the mirror [70]. However, a very small mode size may cause problems in mode matching with other components, such as single-mode optical fibers. Therefore, the mode size should be properly chosen.

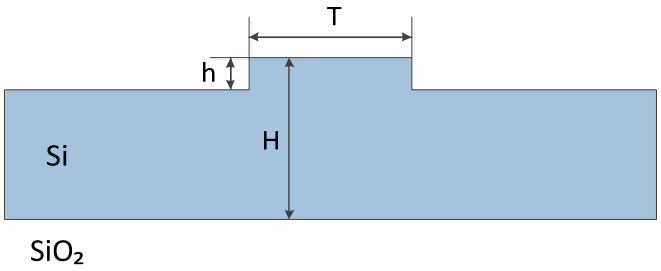

(a)

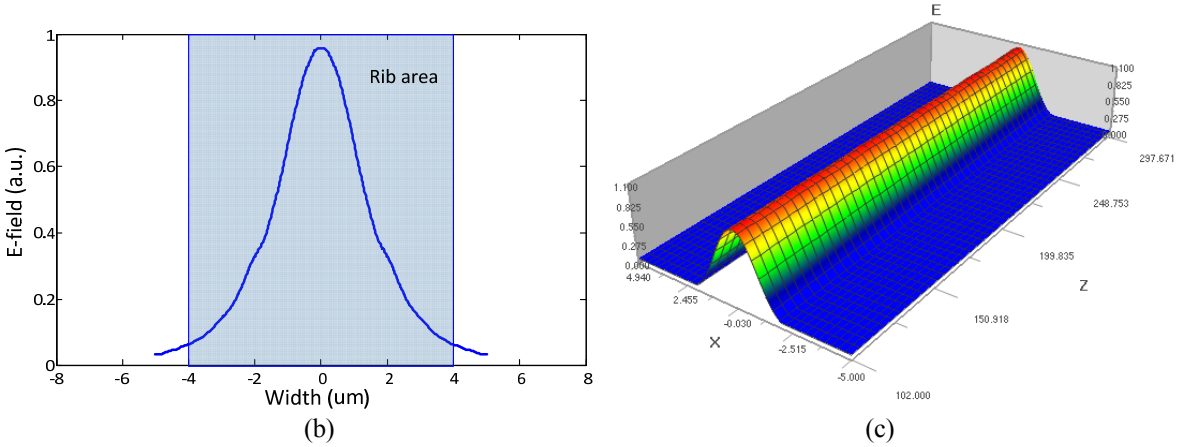

(b) (c)

Figure 3.11 (a) Cross-section of a SOI rib waveguide structure. (b) *Calculated* mode profile for the SOI rib waveguide. (c) Single mode distribution. Refractive indices are 3.4784 for silicon and 1.4443 for silicon dioxide at 1.55 µm.

The designed and fabricated SOI rib guides have the optimized waveguide parameters of $T = 4\ \mu m$, $h = 1\ \mu m$, and $H = 4\ \mu m$. With the given waveguide parameters, the mode field of the SOI rib waveguide is calculated using beam propagation method (BPM). Refractive indices of 3.4784 and 1.4443 are chosen for silicon and silicon dioxide, respectively, at 1.55 μm. Commercial simulation software tool (Optiwave BPM) is used, with the result shown in Figure 3.11(b). Propagation of the mode filed is also calculated, as shown in Figure 3.11(c). It is shown that single-mode operation is well confirmed.

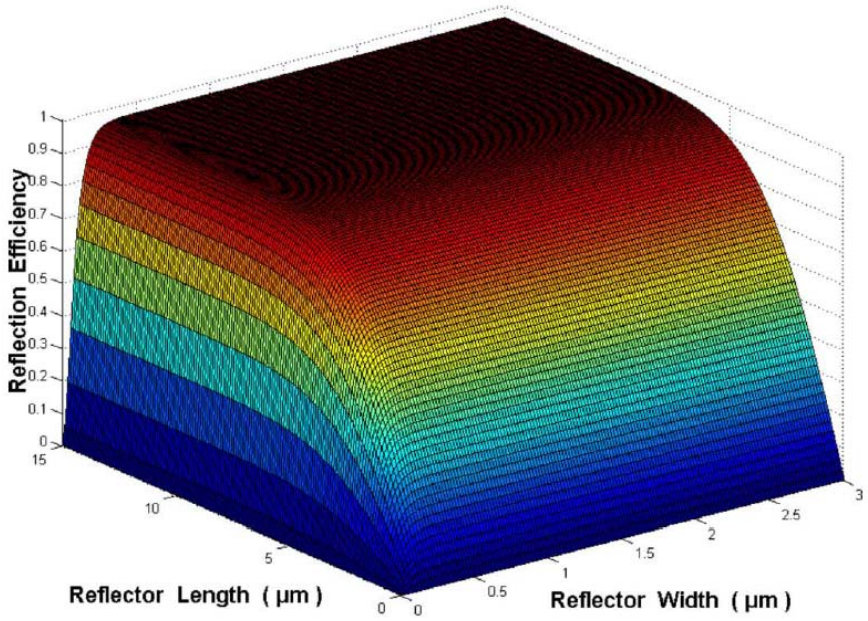

Figure 3.12 Transfer efficiency as a function of reflection mirror dimension (length and width). Reflection angle is 90°, mirror tilt angle is 0°, surface roughness is 100 Å, and shift of mirror is 0.07 μm. (From [69])

In the design of reflection mirror, the following parameters have to be considered accordingly: dimension (the length and width) of the mirror, position (shift to the SOI waveguide), surface roughness and tilt angle of the mirror plane, and material refractive index of the mirror. A comprehensive theoretical model and systematic discussion on the design and optimization of

the reflector for SOI waveguide corner structures have been reported [69]. The combined effect of the most significant physical factors is taken into account.

The dependence of the optical transfer efficiency of the SOI waveguide corner turning mirror structure on the reflector dimension and the corner angle has been analyzed using FDTD method. Figure 3.12 shows the transfer efficiency versus the reflection mirror dimension (length and width) [69]. Here reflector material is air, reflection angle is 90^{o}, mirror tilt angle is 0^{o}, surface roughness is 100 Å, and shift of mirror is 0.07 μm. It is clearly shown that the transfer efficiency of the corner turning mirror can achieve the maximal value of more than 96% at a small reflector size.

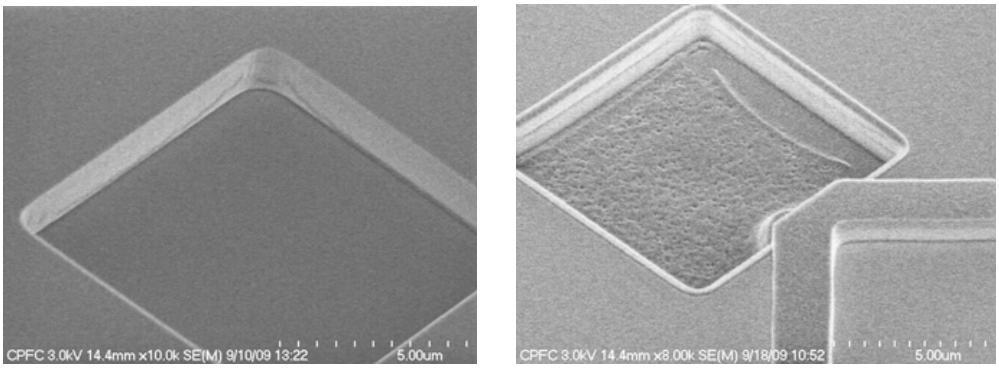

(a) (b)

Figure 3.13 Scanned electrical microscope (SEM) images of feature patterns/structures and measurement evaluations of the fabricated structures. (a) The deep air trench as the mirror; (b) the corner turning structure with the SOI rib waveguide.

According to above optimization, SOI corner turning mirror (CTM) structures with different parameters (reflecting plane shifts of -140, -70, 0, 70, and 140 nm) have been designed and then fabricated in Canadian Photonics Fabrication Centre (CPFC) with support from a fabrication grant of Canadian Microsystems Corporation (CMC). The manufacturing technology for the designed SOI Corner turning mirrors is the high-precision electron-beam lithographic

fabrication with non-contact mask operations. The fabrication quality is evaluated with measurements of the feature values in waveguide dimensions and CTM structure according to the tolerances as shown in Figure 3.13. We can see the SOI rib waveguide has a sharp 90 degree bending at the corner where a square shape mirror structure (the deep air trench) is used. The sidewall verticality of the deep air trench has achieved 90±0.4 degree. Note that for the deep air trench the dimension error is 0.23 μm within 10.0 μm dimension and the sidewall angle error is 0.6° in a 1.5 μm depth.

3.3.2. Measurement Results

The manufactured pattern of SOI double-corner turning mirror structures is shown in Figure 3.14. These structures are the samples used for testing the optical performance improvement of the optimal CTM structure compared with the conventional curved waveguides in PIC systems in this thesis.

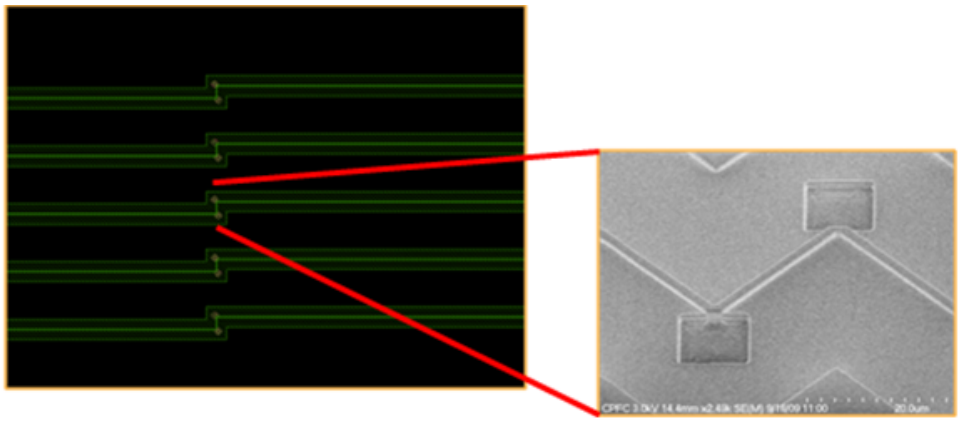

Figure 3.14 Micro-photo images of the CTM structures for measuring the transfer efficiency. The inset shows the double 90 degree corner turning mirror structure.

With the fabricated device, at the wavelength of around 1550 nm, a guided mode output is observed using an infrared camera, as shown in Figure 3.15(a). The losses of the fabricated SOI corner turning mirrors are measured using the experimental setup as shown in Figure 3.3. One group of SOI corner turning mirrors with six different rib sizes of 1.5, 2.0, 2.5, 3.0, 3.5 and 4.0 um are tested. The measurement results of their access losses, which are defined as the difference between the total insertion loss and the propagation loss of the SOI rib waveguides, are shown in Figure 3.15(b). The total insertion loss of the SOI corner turning mirror structure is measured using the cut-back method. The propagation loss of the SOI rib waveguide is estimated by measuring the propagation loss rate of a SOI straight rib waveguide with the same dimension of the corning mirror waveguide, using the previous described Fabry-Perot interference method. In addition, by tuning the polarization controller, the polarization state of the incident light beam can be controlled. Therefore, both TE and TM modes can be obtained.

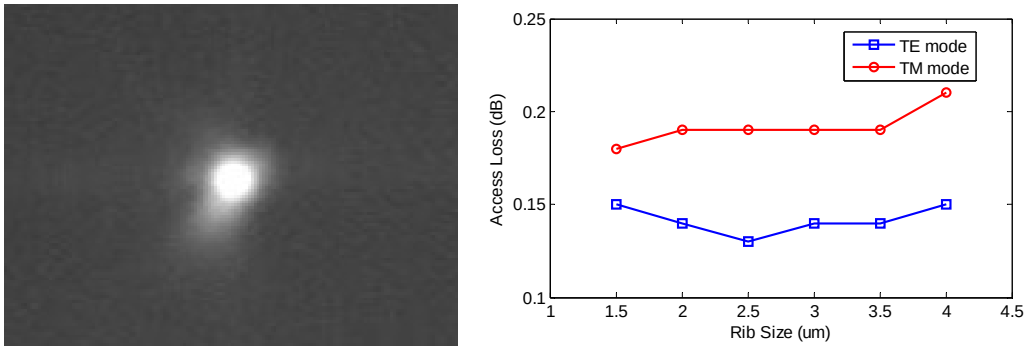

(a) (b)

Figure 3.15 Measurement results of the CTM structures. (a) Measured far-field mode pattern using an infrared camera, veryfying single-mode operation. (b) Access loss of TE- and TM-modes for CTM structures with different rib sizes.

As shown in Figure 3.15(b), both TE- and TM- modes are tested; the polarization dependent loss (PDL) is only 0.05 dB. Another interesting observation is that different rib sizes don't change the access loss obviously.

3.3.3. Discussion and Summary

A large-size SOI rib waveguide corner mirror has been designed. In accordance with our previous work on the modeling and numerical calculation, a serial of corner turning mirror devices with different parameters have been fabricated. In this thesis, we report the experimental measurement results of the fabricated SOI corner turning mirror devices.

With a precision testing station composed of an optical vector analyzer (LUNA system), the optical propagation and access loss of the SOI corner turning mirror structures with different rib sizes have been accurately measured. With the detailed measurements and analyses we obtained that the average propagation loss of each SOI corner mirror structure is 0.14 and 0.19dB for TE and TM polarizations, respectively, resulting in a polarization dependent propagation loss of only 0.05dB. After comparing the results to the SOI curved waveguide structures that studied in Chapter 2, we can reach a conclusion that our innovative SOI corner turning mirror structures can not only significantly reduce the footprint size, but also improve the access loss by replacing the curved sections in any SOI planar lightwave circuit systems.

CHAPTER 4 SOI MULTIMODE INTERFEROMETER BASED 90^{O} OPTICAL HYBRID

Optical 90^{o} hybrids, also known as quadrature optical hybrids, have become the key components in many applications, such as in coherent detection systems, where optical signals with quadrature phase-shift keyed (QPSK) can be demodulated by using optical 90^{o} hybrids and balanced detectors. Optical 90^{o} hybrids can be implemented by using a passive 4 × 4 multimode interferometer (MMI) coupler on a SOI rib waveguide platform. In this Chapter, the concept of 4 × 4 MMI-based optical 90^{o} hybrids will be introduced. Such a device is first studied by numerical simulations using BPM method followed by a detailed experimental measurement of device performance in terms of both amplitude and phase response.

4.1 Introduction to Multimode Interference (MMI) Device

Multimode interference (MMI) devices can perform many different splitting and combining functions and have become very important integrated optical components in photonic integrated circuits. Figure 4.1 shows a schematic configuration (top view) of a simple MMI waveguide with one input port and one output port, which consists of input and output single-mode waveguides and a large dimension multimode waveguide. The key structure of an MMI coupler is the large size waveguide designed to support a large number of guided modes. The width and length of the multimode waveguide are W_{mmi} and L_{mmi}, respectively.

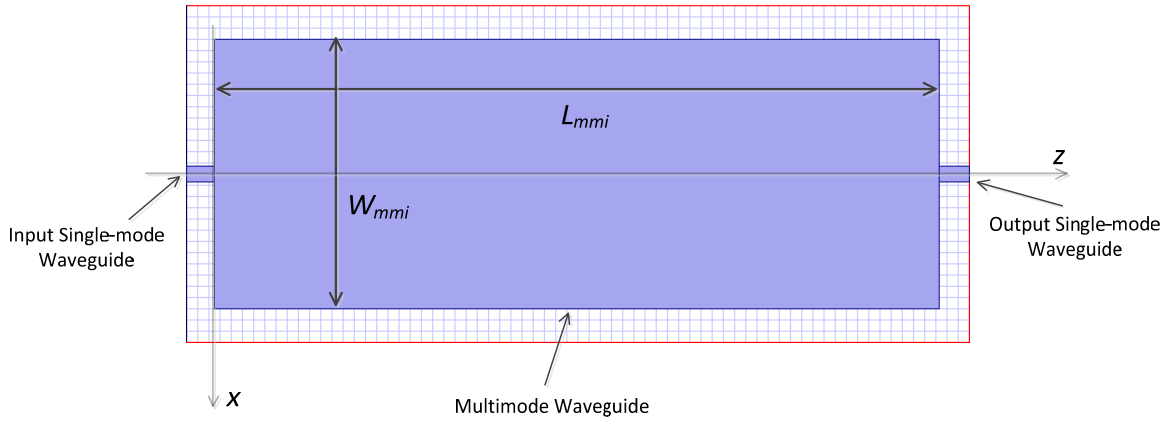

Figure 4.1 Schematic configuration of a 1×1 MMI waveguide.

MMI devices are operating based on self-imaging effect, also known as Talbot effect [71, 72], which generates self-imaging of objects when coherent light beam propagates through the multimode region. The length of the central multimode waveguide is chosen such that the optical field entering from an input waveguide port is self-imaged and produces an array of identical images at the some specific locations. If the output ports are placed at those locations, a MMI device can split the input power into several branches.

Operation of a MMI waveguide coupler can be described as follows. The input light beam excites a large number of optical modes in the central thick coupling region. Each of the modes propagates with a slightly different propagation constant. For example, the *m*-th TE mode in the multimode waveguide is expressed by [31]

$$E_y^m(x,z)=\begin{cases} A_m\cos\left(u_m+\dfrac{m\pi}{2}\right)\exp\left[\dfrac{2\omega_m}{W_{mmi}}\left(x+\dfrac{W_{mmi}}{2}\right)-j\beta_m z\right], & x<-\dfrac{W_{mmi}}{2} \\ A_m\cos\left(\dfrac{2u_m}{W_{mmi}}x-\dfrac{m\pi}{2}\right)\exp\left(-j\beta_m z\right), & |x|\le\dfrac{W_{mmi}}{2} \\ A_m\cos\left(u_m-\dfrac{m\pi}{2}\right)\exp\left[-\dfrac{2\omega_m}{W_{mmi}}\left(x-\dfrac{W_{mmi}}{2}\right)-j\beta_m z\right], & x>\dfrac{W_{mmi}}{2} \end{cases} \quad (4\text{-}1)$$

Since the propagation constant of the m-th mode can be expressed as $\beta_m = \sqrt{k^2 n_{eff}^2 - \left(2u_m / W_{mmi}\right)^2} \cong kn_{eff} - \frac{(m+1)^2 \lambda}{4n_{eff} W_{mmi}^2}\pi$, then the total electric filed in the MMI waveguide region ($|x| \le \frac{W_{mmi}}{2}$) is obtained by

$$\Psi(x,z) = \sum_{m=0}^{M-1} E_y^m(x,z) = \exp(-jkn_{eff}z) \sum_{m=0}^{M-1} A_m \cos\left(\frac{(m+1)\pi}{W_{mmi}}x - \frac{m\pi}{2}\right) \times \exp\left(j\frac{(m+1)^2 \pi\lambda}{4n_{eff}W_{mmi}^2}z\right) \tag{4-2}$$

where M is the total number of all supported modes. We can define the characteristic length $L_C = \frac{4n_{eff}W_{mmi}^2}{\lambda}$. Then the electric field at the MMI characteristic length L_C is obtained as

$$\Psi(x, L_C) = \exp\left[-jkn_{eff}L_C + j(m+1)^2 \pi\right]\Psi(x,0) \tag{4-3}$$

It is easily confirmed from equation (4-3) that the input field will be reproduced (self-imaged) at the characteristic length L_C with slight phase change. In general, the quality of self-imaging effect is dependent on the number of supported modes, the confinement of the multimode waveguide, and the waveguide birefringence.

This self-imaging feature in an MMI waveguide has been verified by numerical simulations using the BPM method. Figure 4.2 shows the self-image formation for light beam input at the center of the MMI waveguide. We can see that an image of the input electric field is reproduced at the characteristic length of the MMI waveguide. Note that depending on the MMI waveguide length, multiple images of the input field can also be generated on the output end if the

waveguide length is less than the characteristic length L_C. It is interesting that N images are formed at specific location of $z = L_C / N$, for any integer N. Therefore, by properly choosing the coupler length, on can design $1 \times N$ power splitters based on the MMI concept.

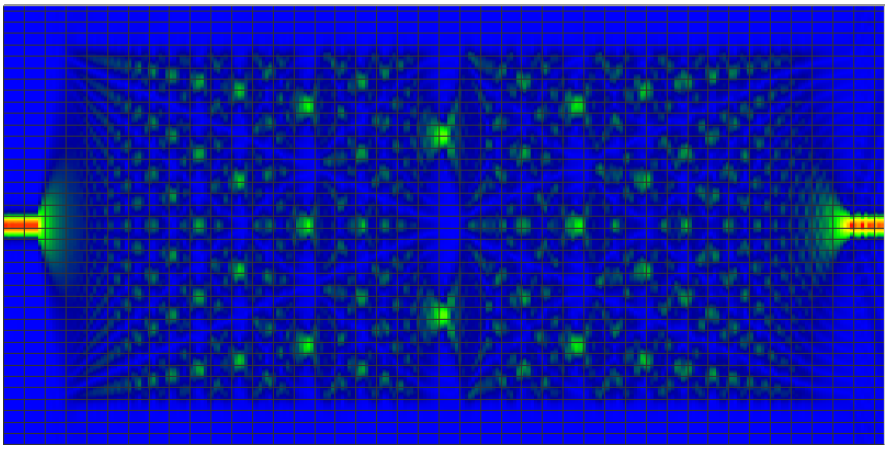

Figure 4.2 Numerically simulated intensity evolution of a 1×1 MMI waveguide over a characteristic length showing formation of multiple images at certain locations. The light is input at the center of MMI waveguide. Simulation is performed using the BPM method (OptiBPM tool).

4.2 Optical 90^o hybrids based on SOI 4 × 4 MMI Coupler

Optical 90-degree hybrid is a six-port device (with two inputs and four inputs) used for coherent signal demodulation in fiber optic communications systems. In a coherent signal demodulation system, the quadrature phase-shift keyed (QPSK) signal (S) and the local oscillating (L) are incident to the optical hybrid. At the outputs, the hybrid provides four linear combination of the signal with the reference which differs by a relative phase shift of the reference of 90º. That is, the output phase relations are given by $S + L$, $S - jL$, $S + jL$ and $S - L$. The four output signals are detected by a pair of balanced detectors to provide in-phase and quadrature (I&Q) channels of the QPSK signal.

MMI based integrated optical hybrids have been intensively investigated over a wide ranges of technologies. For example, optical 90-degree hybrid can be realized using 2 × 2 MMI couplers plus a phase shifting device, which is used to achieve the required phase relation at the output of the 2 × 2 coupler [73, 74]. The advantage of this approach is that the phase relation at the output of the MMI waveguide coupler is reconfigurable and can be controlled very accurately. However, since an addition phase control circuit is required, extra power dissipation and increased footprint are caused. On the other hand, the optical 90-degree hybrid can be realized using a fully passive 4 × 4 MMI coupler that intrinsically offers the required phase relations between the output ports. In this thesis, optical 90-degree hybrids based on 4 × 4 MMI couplers are studied theoretically and experimentally.

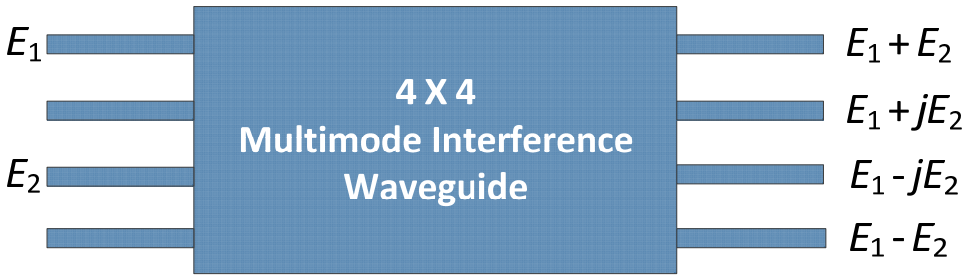

Figure 4.3 Schematic of a 4 × 4 MMI coupler configured as an optical 90-degree hybrid. Input fields E_1 and E_2 are incident at input ports 1 and 3, respectively.

An optical 90-degree hybrid can be implemented using a 4 × 4 MMI waveguide coupler, when the signals are present only at input ports 1 and 3, as shown in Figure 4.3. The required phase relation arises naturally at the output ports of an ideal 4 × 4 MMI waveguide coupler. Let the input fields incident to two input ports are E_1 and E_2, respectively. At the output of the optical hybrid generates a linear combination of the two input fields, with a relative phase shift between

two input fields of 0, π/2, 3π/2, and π. Ideally, if perfect power balance between all the output ports is satisfied and any constant phase offset is neglected, the output fields are proportional to $E_1 + E_2$, $E_1 + jE_2$, $E_1 - jE_2$, and $E_1 - E_2$, respectively. By sending channel 1 and 4 to one balanced photodetector, and channel 2 and 3 to another balanced photodetector, the in-phase and quadrature (I&Q) terms of the QPSK signal can be demodulated. Note that to direct the output ports to the correct balanced receivers, a waveguide cross over will be required. To overcome this problem, a new structure applying a *2* × *4* MMI coupler, a phase shifter and a *2* × *2* MMI coupler has been reported recently [75]. However, the device gets more complicated.

Here the principle of MMI coupler based optical hybrid is briefly described. From the discussion in Section 4.1, we know that *N* images are formed at specific location of $L_N = L_C / N$, for any integer *N* (in our case, $N = 4$), where L_C is the characteristics coupling length of the MMI waveguide. Consider an *N* × *N* MMI waveguide coupler, inputs are numbered with indices *i*, and output are numbered with indices *j*. The phase relation for imaging input *i* to output *j* can be expressed in a compact form as [76]

$$\varphi_{i,j} = \begin{cases} \varphi_0 + \pi + \dfrac{\pi}{4N}(j-i)(2N-j+i), & i+j \text{ even} \\ \varphi_0 + \dfrac{\pi}{4N}(j+i-1)(2N-j-i+1), & i+j \text{ odd} \end{cases} \tag{4-4}$$

where φ_0 is the constant phase given by $\varphi_0 = -kn_{eff}L_N = -\dfrac{\pi}{N} - \dfrac{\pi}{4}(N-1)$. It is easily reach a conclusion that an ideal 4 × 4 MMI waveguide coupler can function as an optical 90-degree hybrid.

4 × 4 MMI waveguide couplers have been previously implemented in glass stripe waveguides [72], in InP platform [77], and in 4μm silicon-on-insulator (SOI) waveguides [78]. Most recently, our group has reported a more compact optical 90-degree hybrid, which is built on smaller size SOI waveguide technology (1.5 μm SOI -based rib waveguide, with 0.8μm rib height) [79]. In this thesis, 4 × 4 MMI waveguide coupler based optical 90-degree hybrids are studied by both simulations and experimental measurements.

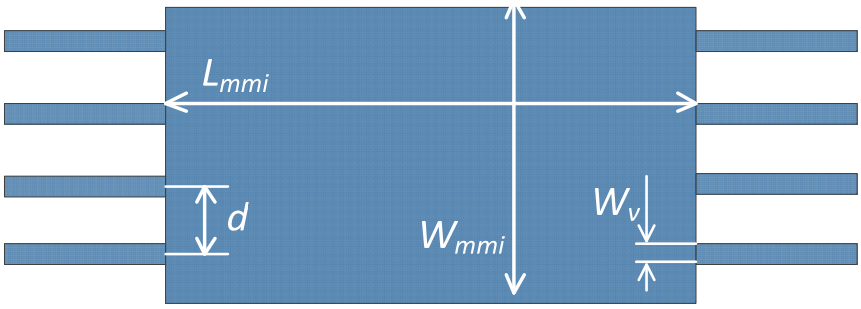

Figure 4.4 The geometry of a 4 × 4 MMI coupler.

The geometry of the designed 4 × 4 MMI waveguide coupler is shown in Figure 4.4. The parameters of the MMI device are listed below: the length and width of the multimode waveguide are L_{mmi} and W_{mmi}, respectively, the rib waveguide width is W_V, and the center-to-center spacing between two adjacent waveguides is d. Note that the spacing should be large enough to avoid the power coupling between adjacent SOI rib waveguides. Then the minimum width of the multimode waveguide should be determined according to cover all the 4 waveguide channels. The length of the multimode waveguide must be carefully selected to satisfy the self-image conditions. For a 4 × 4 MMI waveguide, an estimate of the MMI length is given by

$$L_{mmi} = \frac{L_C}{4} = \frac{n_{eff} W_{mmi}^2}{\lambda} \tag{4-5}$$

Based on the considerations above, 4 × 4 MMI waveguide couplers are designed using the Kalistos optimizer [79]. The parameters of the MMI waveguide are summarized in the following table. Figure 4.5 shows the example layout of mask design for a 4 × 4 MMI waveguide coupler, using the DW-2000 mask layout design tool. Extension taper waveguides at the input and output ports of the MMI coupler are also designed to achieve optical coupling from lasers and to photodetectors.

TABEL 4.1. PARAMETERS OF 4 × 4 MMI WAVEGUIDE

Parameters	Value (in μm)
Length of MMI (L_{mmi})	3715.8
Width of MMI (W_{mmi})	40.296
Width of rib waveguide (W_V)	4
Waveguide spacing (d)	10.222

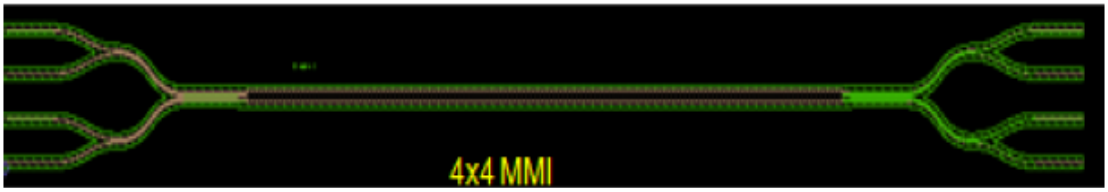

Figure 4.5 Example layout of design mask for a 4 × 4 MMI coupler. From [79].

4.3 Simulation using BPM Method

The performance of 4 × 4 MMI coupler based optical 90-degree hybrids is first studied by numerical simulations using BPM method (OptiBPM tool). The parameters listed on Table 4.1 are chosen in the simulations. Both the power distribution and phase relation between the four output ports are studied.

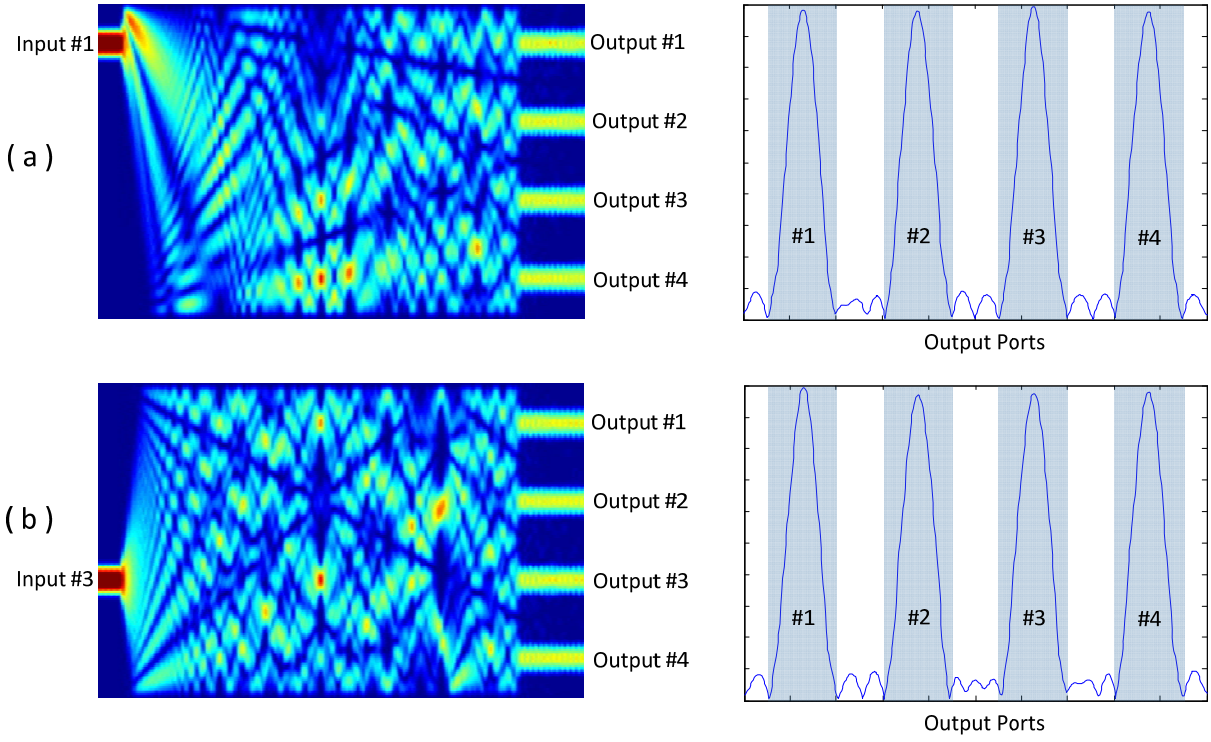

Figure 4.6 Electric field distributions and output signals for two cases. (a) Input presents at port #1, and (b) input presents at port #3.

Simulations are implemented in two separate steps: in each step, the input optical field is present at only one of the input ports (#1 and #3). Results obtained from the two steps are compared to evaluate the performance of the 4×4 MMI coupler based optical hybrid. Figure 4.6 shows the electric field distributions and output signal in both cases. In this case, the input

wavelength of 1550 nm is selected. We can see that the input optical fields have been equally distributed to the four output ports due to the self-imaging effect. Table 4.2 summarizes the power split ratio.

TABEL 4.2. ELECTRIC FIELD DISTRIBUTION RATIO IN 4 × 4 MMI

Output Ports	Power Ratio (Input #1)	Power Ratio (Input #3)
Port #1	0.2455	0.2483
Port #2	0.2444	0.2420
Port #3	0.2482	0.2432
Port #4	0.2442	0.2445

The phase distributions are also simulated when the input field excites the input port #1 and #3, respectively. The input optical signal has a wavelength of 1550 nm. The simulation results of both cases are shown in Figure 4.7. The phases of the optical signal at all the four output ports are also plotted.

TABEL 4.3. PHASE RELATIONS AT OUTPUT PORTS OF 4 × 4 MMI

Output Ports	Phase in degree (Input #1)	Phase in degree (Input #3)	Phase Relation in degree
Port #1	48.01	-177.42	134.57
Port #2	2.73	47.45	44.72
Port #3	-177.39	48.54	225.93
Port #4	46.92	2.71	-44.21

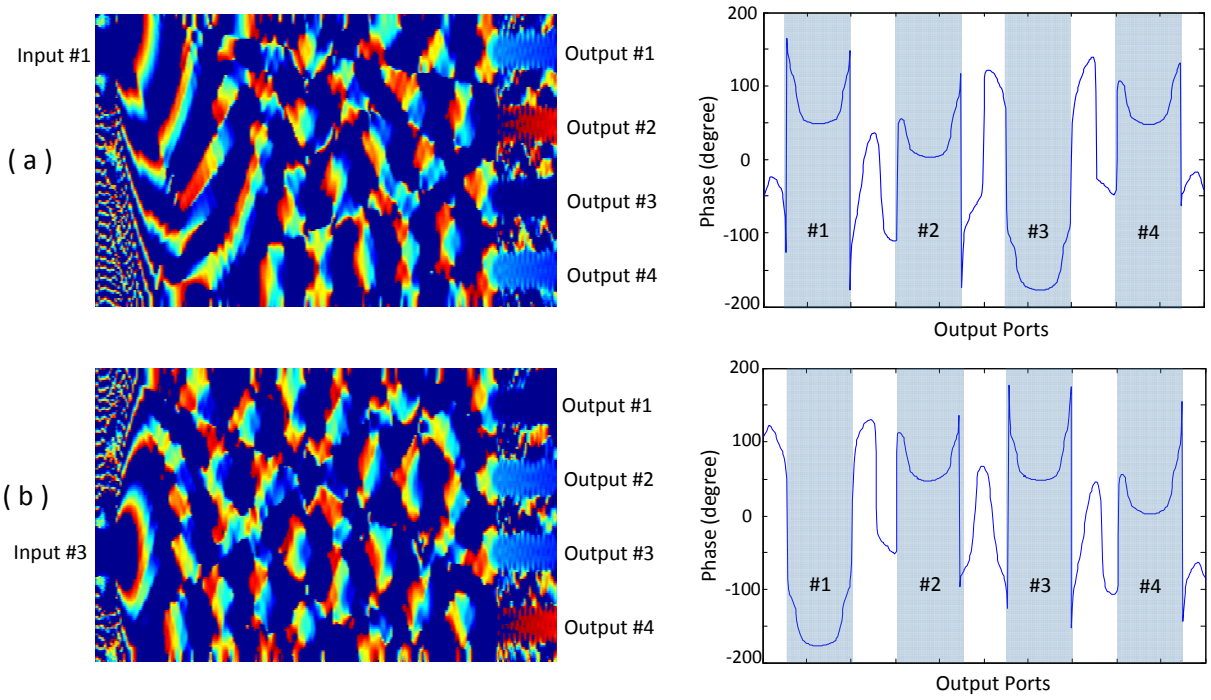

Figure 4.7 Phase distributions and phase relation for both cases. (a) Input field presents only at port #1, and (b) input field presents only at port #3.

Table 4.3 summarizes the phase relation between the four output ports when the input field excites the input port #1 and #3. We can find that the phase differences between the output port #1 and other three output ports are 89.85°, -90.36°, and 178.78°, respectively, which matches very well with the desired values of $\pi/2$, $3\pi/2$, and π.

It is preferred that an optical hybrid can work over broadband spectral range in the telecommunications band (~1550 nm). The wavelength dependence of the output phases is also studied. Numerical simulations are conducted using BPM method with the wavelength varying over 20 nm bandwidth (from 1540 to 1560 nm). The corresponding results are plotted in Figure 4.8. Across the 20 nm bandwidth, the output phases remain stable with a maximum drift of 0.12

radian, which verifies the broadband performance of the 4 × 4 MMI coupler based optical hybrid.

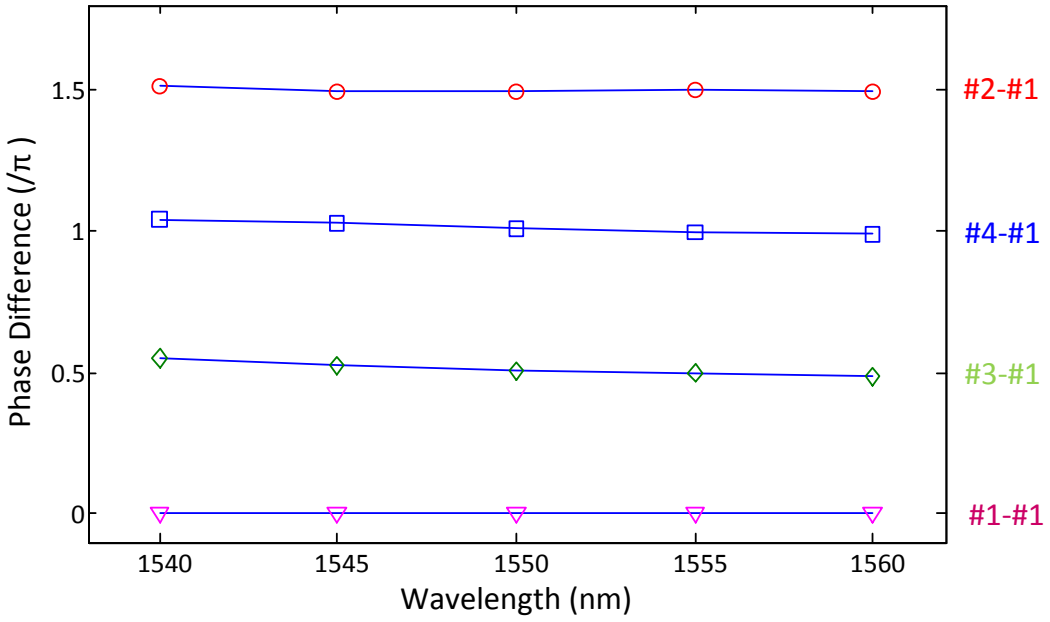

Figure 4.8 Relative phase differences at the output ports with respect to port #1.

4.4 Measurement Results

The designed compact 4 × 4 MMI coupler has been fabricated at the Canadian Photonics Fabrication Centre (CPFC). The MMI devices are fabricated in SOI rig waveguides with top silicon width of 1.5 μm and a rib height of 0.8 μm. In this Section, experimental measurement results demonstrating broadband quadrature phase behavior of the compact SOI 4 × 4 MMI couplers are presented. The measurement results verify the potential application of SOI-waveguide-based optical 90^{o} hybrid in a coherent optical receiver.

Principle of Phase Measurement

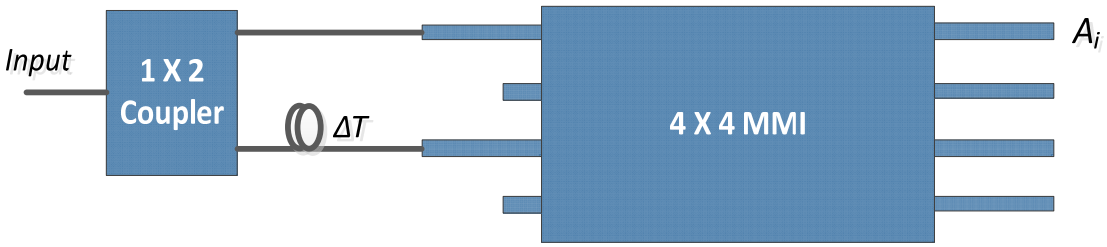

Figure 4.9 Concept of phase measurement of 4 × 4 MMI coupler based on an optical interferometer.

Although phase information can be easily obtained from numerical simulations, direct measurement of optical phase responses of different output ports is quite challenging. A feasible method to measure phases is based on optical interference measurement. The concept of measurement system is shown in Figure 4.9. A 1 × 2 optical coupler is used to split the input optical signal into two arms and form a Mach-Zehnder interferometer. A constant time delay ΔT is introduced in one of the arms. Therefore, a spectral interference fringe is obtained with the free spectral range (FSR) determined by the time delay. When we measure the interfered signal at the output ports, different phase shifts are introduced by the 4 × 4 MMI coupler. The optical signal at the *i*-th output port is given by

$$A_i(\lambda) = \alpha\left[1+\cos\left(2\pi\frac{\Delta T\times c}{\lambda_0^2}\lambda+\varphi_i\right)\right] \tag{4-6}$$

where α is the attenuation coefficient, λ_0 is the central wavelength, c is the light velocity in vacuum, and φ_i is the phase different between the two input ports, measured at the *i*-th output port. The interference fringes are spectrally shifted due to the constant phase shifts. By analyzing the interference fringes at different output ports, phase relation of the 4 × 4 MMI coupler can be determined by using Fourier transform [80] or Hilbert transform [81] algorithms.

Measurement Setup

To evaluate the phase behavior of 4×4 MMI couplers, we construct a 4×4 delayed interferometer based on the MMI coupler, as shown in Figure 4.10. A fiber-based beam splitter (BS) is used to divide the input signal into two paths. Only input ports #1 and #3 of the 4×4 MMI coupler are used. The length difference of the two input fibers to ports #1 and #3 is properly selected such that the implemented interferometer has a free-spectral range (FSR) of ~0.5 nm, according to equation (4-6).

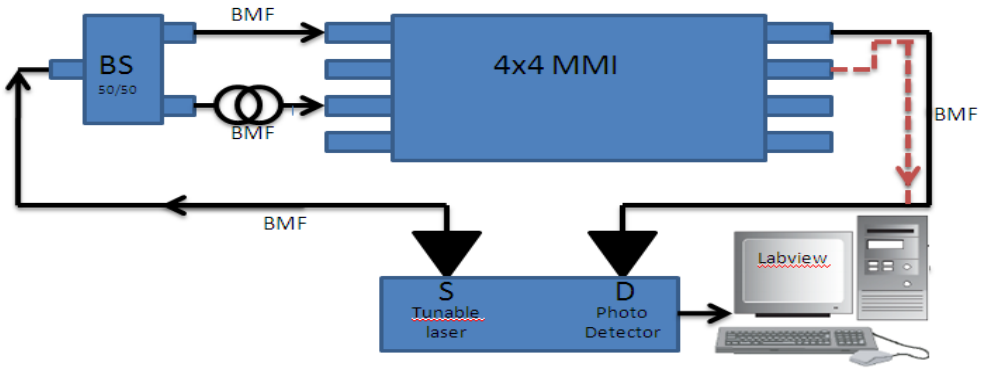

(a)

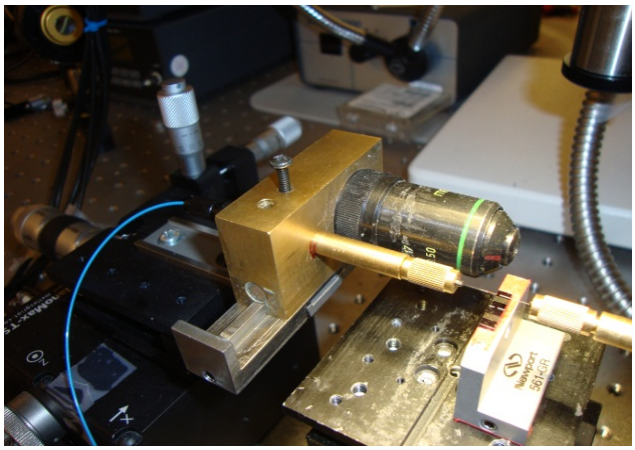

(b)

Figure 4.10 (a) Test bed setup to measure the phase relation of a 4×4 MMI based on a delayed interferometer (DI). BS: beam splitter. (b) Picture showing the coupling between fiber and MMI waveguide.

The interference fringe at each output port is measured in the spectral domain. The phase shifts between these interference fringes represent the phase differences at the output ports with respect to the reference port. The measurement is implemented by sweeping the wavelength of the input optical signal and monitoring the transmitted optical power at each output port. A tunable laser source and a photo detector are controlled by a PC running Labview program to perform the measurement in a fast and accurate manner. It is known that the delayed interferometer is usually very sensitive to environment disturbances, such as temperature change, table vibration, or air flow. Therefore the measurement is should be implemented within a short period of time.

Measurement Results using A Tunable Laser

A tunable laser source is used in the measurement. The wavelength of the input signal is fast tuned over a broad spectral range (~20 nm) with a constant step of 0.02 nm. Waiting time for wavelength sweeping is 0.5 s, which is selected to achieve fast measurement but still maintain good stability for each optical wavelength.

Figure 4.11(a)-(d) show the measured transmission spectra of the fabricated 4 × 4 MMI coupler device at four output ports employing the testing setup as shown in Figure 4.10. Output transmission spectra from each output port varied sinusoidally over a 20-nm bandwidth (1540-1560 nm) in accordance with the phase differences at the delayed interferometer. The inset in Figure 4.11(a) shows the zoom-in view of the spectral interference fringe of output port #1 at vicinity of 1543 nm, which clearly verifies an FSR of 0.52 nm. Note that the transmission spectrum was measured only for a single polarization (linearly polarized transverse-electric (TE) mode). Transverse-magnetic (TM) mode performance is comparable according to our

previous simulations, proving that the MMI device is polarization-independent. Experimental evaluation of MMI performance for TM mode will be implemented in the future and beyond the scope of this thesis.

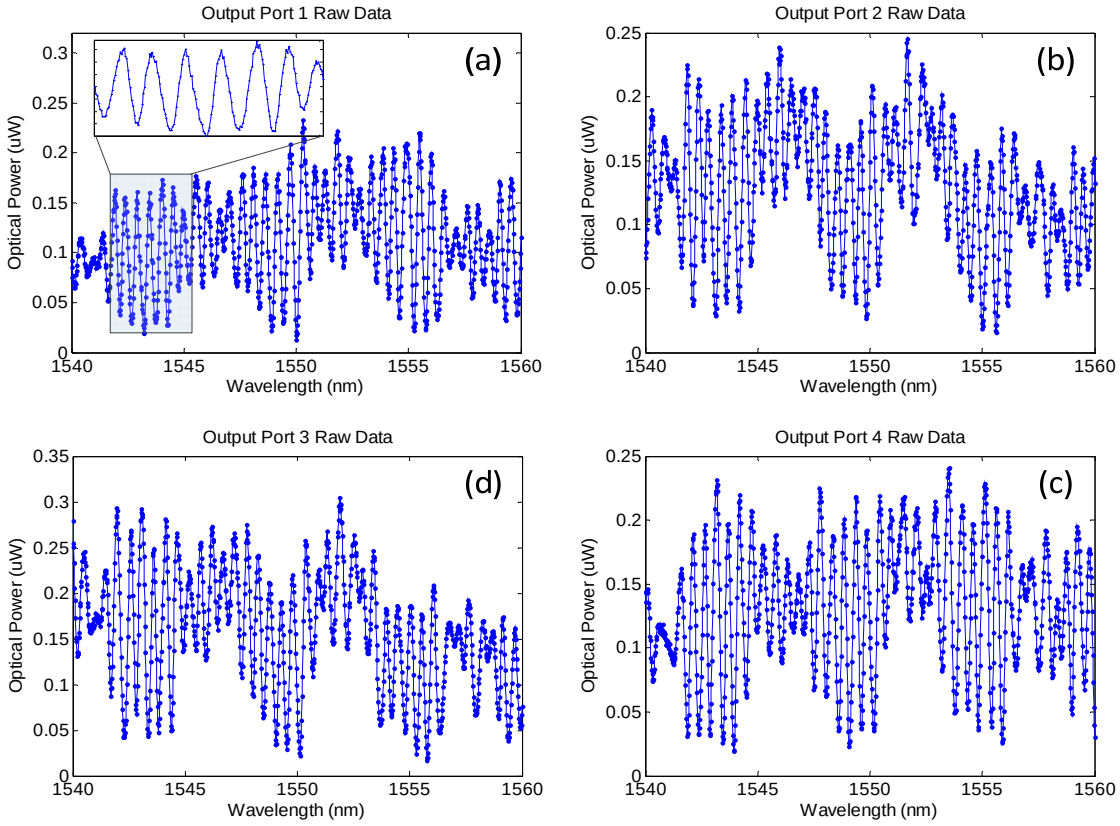

Figure 4.11 Measured transmission spectra for TE mode at four output ports of the 4 × 4 MMI coupler.

To evaluate the wavelength dependence of the output phases and to compare the phases of different output ports, the phase information of spectral interference fringe at each output port is extracted using digital Hilbert transform [81], with the results plotted in Figure 4.12(a). The inset in Figure 4.12(a) shows the phases of four output ports at vicinity of 1550 nm. Relative phases at the output ports with respect to port #1 are shown in Figure 4.12(b). Phase differences between port #2 and port #3, port #1 and port #4 are plotted in Figure 4.12(c) and (d),

respectively. The red dashed lines show the desired phase shift value. We are able to observe π-phase differences between the in-phase ports (#1 and #4) and the quadrature ports (#2 and #3).

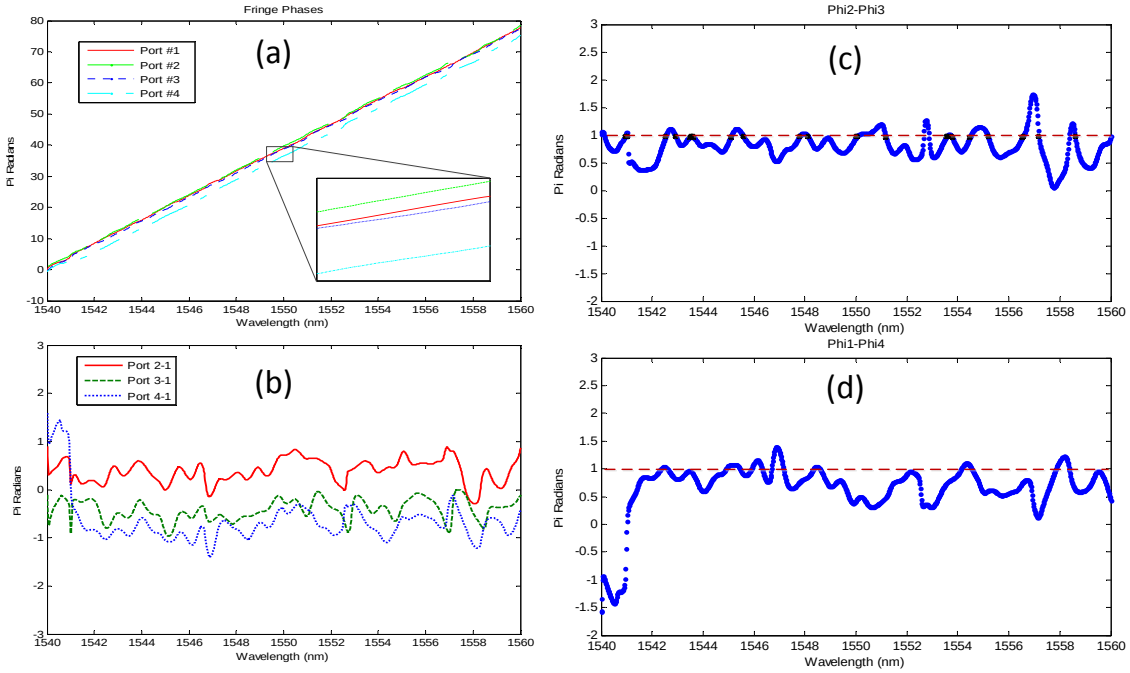

Figure 4.12 Measured phase behavior of the 4 × 4 MMI coupler. (a) Extracted phases at the four output ports, (b) relative phases at the output ports with respect to port #1, (c) phase difference between output #2 and output #3, (d) phase difference between output ports #1 and #4.

As seen in Figure 4.12, phase relationship among different output ports remains stable across the 20-nm spectral bandwidth. The phase variations on the traces in the Figure are mainly attributed to the variations of input and output coupling, which is not implemented on the experimental on-chip. Integrating beam splitter, input optical waveguides and the 4×4 MMI device on a single chip will greatly improve the measurement accuracy.

Measurement Results using Luna System

To improve the measurement accuracy, an optical vector analyzer (Luna System) is used to replace the tunable laser source and the photodetector. As a result, the broadband spectral interference fringes can be measured in a faster and more accurate manner. Figure 4.13 shows the measured transmission spectrum at the output port # of the 4 × 4 MMI coupler over a 90-nm spectral range (from 1525 to 1615 nm). The effective spectral resolution of the measurement offered by Luna system is about 3 pm. Inset shows the zoom-in view of the spectral interference fringe at vicinity of 1550 nm. We can find that amplitude variation and phase shifts are observed over during the wavelength scanning. However, within a relatively narrow bandwidth (or equivalently a short measurement time), clear sinusoidal spectral interference fringes can be obtained, which may lead to more accurate measurement of phase behavior of the 4 × 4 MMI coupler.

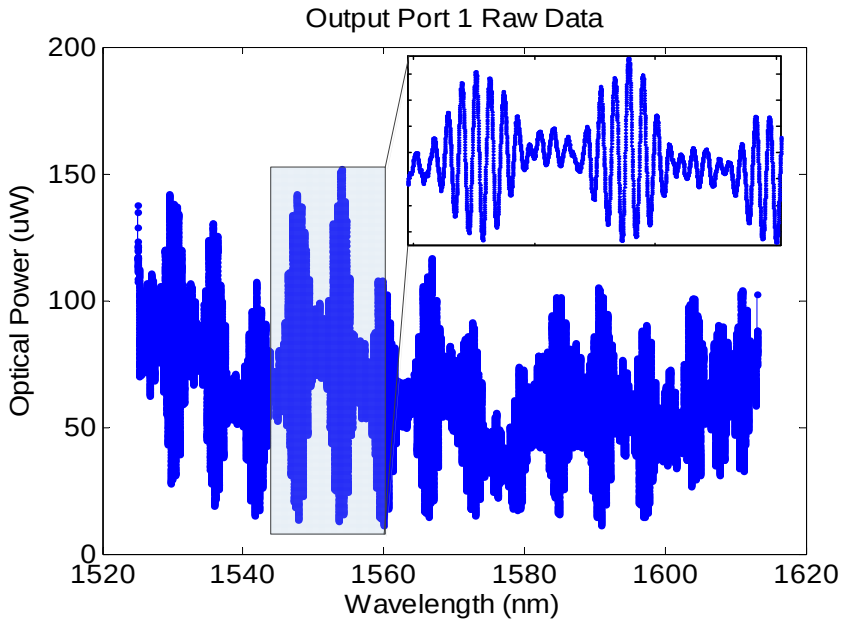

Figure 4.13 Measured transmission spectrum at the output port # of the 4 × 4 MMI coupler over a broad spectral range (90 nm). Inset shows the zoom-in view of the spectral interference fringe at vicinity of 1550 nm.

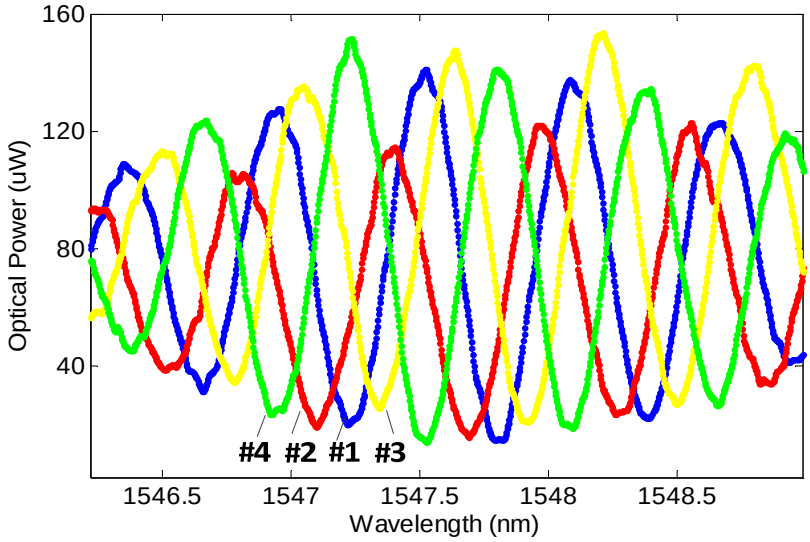

Figure 4.14 Interference fringes measured at all the output ports. Labels indicate the respective port.

The interference fringes at all the output ports are measured using the Luna system, with the results shown in Figure 4.14, where filter characteristics over 3-nm bandwidth is plotted. The labels indicate the respective output port. We can see that spectral shifts of almost half of the FSR are observed, indicating the desired $\pi/2$ phase shifts between the output ports.

Hilbert transform algorithm is applied again to reconstruct the phase information of the measured spectral interference fringes, with the results shown in Figure 4.15. We can clearly see that improved phase relation is obtained within a relatively narrow bandwidth (~ 3 nm), thanks to the use of Luna system. Improved phase measurement can also be implemented at different spectral ranges with similar optical bandwidth (~3 nm). Figure 16 shows the measured relative phases at the output ports with respect to port #1 over a 3-nm bandwidth (from 1552.5 to 1555.5 nm), verifying the quadrature phase behavior of the 4 × 4 MMI coupler.

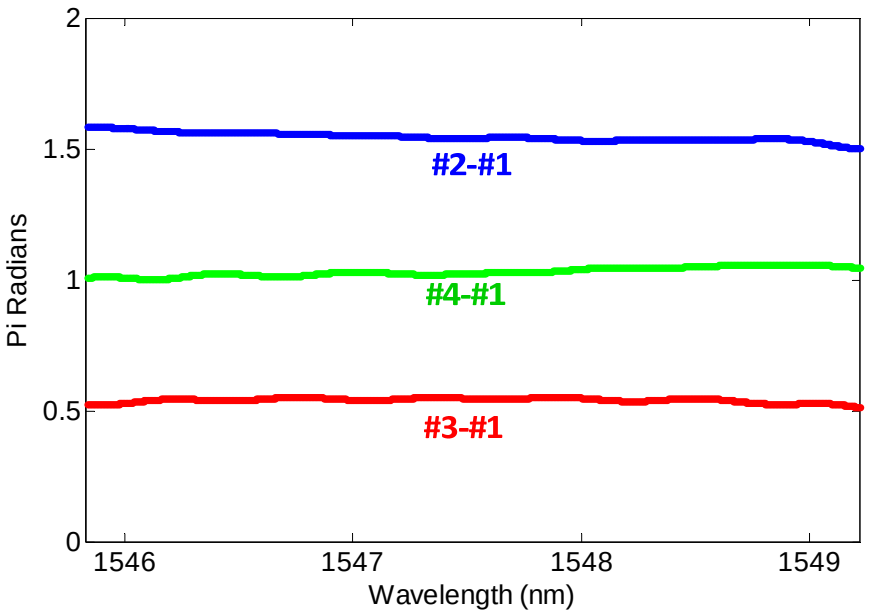

Figure 4.15 Measured relative phases at the output ports with respect to port #1 over a 3-nm bandwidth (from 1546 to 1549 nm)..

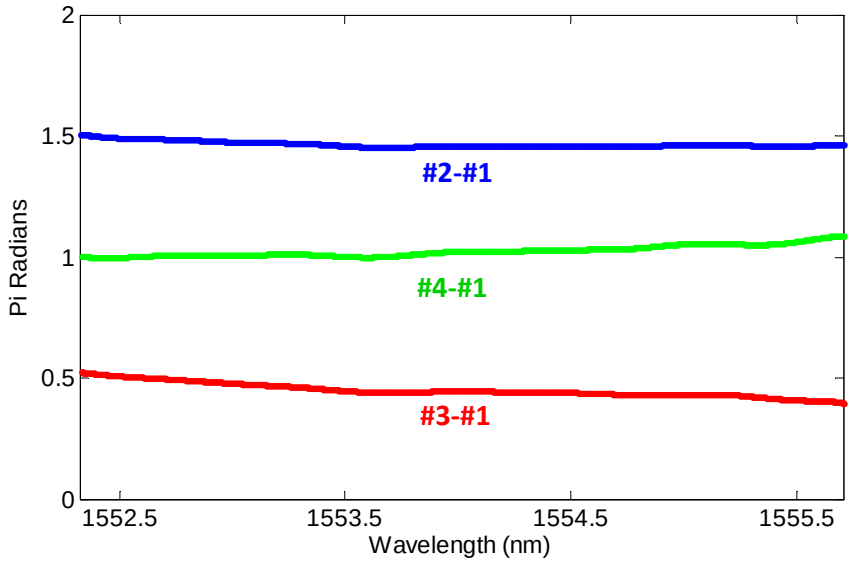

Figure 4.16 Measured relative phases at the output ports with respect to port #1 over a 3-nm bandwidth (from 1552.5 to 1555.5 nm).

4.5 Discussion and Summary

In this Chapter, a compact SOI-based 4×4 MMI coupler was tested with an emphasis on phase performance. The measurements are implemented based on a delayed interferometer. The key issue is to carry out the measurements fast and accurately. Tunable laser was first used to scan a 20-nm wide spectral range. Quadrature optical phase behavior was observed over the 20-nm spectral range around 1550-nm. However, moderate phase errors are observed, which are mainly attributed to the variations of input and output coupling during the measurement process (a few minutes).

To improve the measurement accuracy, an optical vector analyzer (Luna system) is then used to perform the measurement in a faster and more accurate manner. Phase behavior of the MMI coupler over a much more broad spectral range (from 1525 to 1615 nm) was characterized. While phase variations still present during the measurement, superior phase relation was obtained with relatively narrow spectral bands. To ensure good measurement over the whole bandwidth and to greatly improve the measurement accuracy, all the discrete optical devices, such as beam splitter, input optical waveguides and the 4 × 4 MMI device, should be integrated on a single chip.

In summary, 4 × 4 MMI couplers have been realized in SOI rib waveguide technology. Optical phase quadrature behavior of the MMI coupler has been experimentally characterized. Our demonstration verifies its functionality as a passive optical 90^{o} hybrid and its application in digital optical coherent receivers.

CHAPTER 5 CONCLUSIONS

5.1 Thesis Summary

Silicon-on-insulator (SOI) waveguides have become a significant part of photonic dense integrated circuits. In this thesis, the research efforts have been focused on the performance characterization of passive SOI waveguide devices.

The first group of SOI waveguide devices under investigation is curved waveguides and corner turning mirrors. Low-loss SOI curved waveguides are attracting attention as they offer solutions to the dominant issue of integration density of photonic integrated circuits on a single SOI chip. Propagation loss and radiation loss rate of SOI curved waveguides are accurately measured by using Fabry-Perot interferometric method with the help of an optical vector analyzer (Luna system). The presented technique provides a universal solution for optical loss measurement of photonic integrated chips. However, the minimum acceptable radius curvature of the SOI rib curved waveguide bend structure is quite large. As a solution to this problem, SOI corner turning mirror (CTM) structures based on total internal reflection have been studied. The optical propagation loss and polarization dependent loss of SOI CTM structures have been measured using an optical vector analyzer (Luna System). The testing results show that the innovative SOI CTM structures can not only significantly reduced the footprint size of the SOI chip, but also improve both the propagation loss and polarization dependent loss by replacing the curved sections in SOI photonic integrated circuit systems.

The second SOI waveguide device under test is a 4 × 4 MMI coupler. Performance of the MMI coupler and its utility in optical 90^o hybrid were studied in both numerical simulation and experimental measurements, with an emphasis on phase relation measurement. From the simulation and experimental results, it is concluded that Quadrature optical phase behavior was observed over a 20-nm-wide spectral range around 1550-nm, verifying its functionality as an optical 90^o hybrid and its application in digital optical coherent receivers.

5.2 Major Contributions

Performance of SOI waveguide devices have been studied in this Thesis. Numerical simulation methods, such as FDTD and BPM, have been used to simulate the designed SOI rib waveguide devices. The mode field, power distribution, and complex spectral response of the devices have been calculated, with good agreements with theoretical analysis.

The author performed all the measurements and characterization of the devices. To accurately characterize the performance of the SOI waveguide devices, a complete SOI chip testing setup has been built. System parameters, such as coupling conditions, data acquisition settings and digital processing algorithm, have been optimized. Specifically, a Fabry-Perot interference method has been analyzed and implemented to measure the propagation loss of SOI rib waveguides. A delayed interference method was employed to measure the phase behavior of the 4 × 4 MMI couplers. An optical vector analyzer (Luna System) was used to improve the measurement accuracy. For example, in both Fabry-Perot interference and delay measurements, broadband spectral response (interference fringe) of the SOI devices was measured with a high spectral resolution of 3 pm. In addition, the broadband measurements were performed in a fast manner (less than 1 s), such that the environment disturbances to the interferometers can be

greatly reduced. Good agreement between simulated and experimentally measured results gives us confidence that the designed SOI devices can deliver their function in practical applications.

The original contribution of this research work has been evidenced by the following publications and presentations in scientific and engineering journals and conferences.

Publication List

1 H. Nikkhah, **Q. Zheng**, I. Hassan, S. Abdul-Majid, T. J. Hall, "Free space and waveguide Talbot effect: phase relations and planar light circuit applications," *Photonic North 2012*, 6-8 June 2012, Montreal, QC, Canada.

2 S. Abdul-Majid, I. Hasan, **Q. Zheng**, S. Bidnyk and T. J. Hall, "90° SOI Optical Hybrid for Radio-over- Fiber Links," Annals in Telecommunication, accepted.

3 D. G. Sun, Z. Hu, S. Abdul-Majid, R. Vandusen, **Q. Zheng**, I. Hasan, T. G. Tarr, S. Bidnyk, and T. J. Hall, "Limitation Factor Analysis for Silicon-on-Insulator Waveguide Mach-Zehnder Interference based Electro-Optic Switch," *IEEE/OSA Journal of Lightwave Technology*, vol. 29, no. 17, pp. 2592-2600, Sep. 2011.

4 **Q. Zheng**, D. G. Sun, I. Hasan, S. Abdul-Majid and T. J. Hall, "An Accurate Measurement Method for Optical Radiation Loss of Silicon-on-Insulator Curved Waveguides," *7th International Workshop on Fibre Optics and Passive Components* (WFOPC 2011), 13-15 July 2011, Montreal, Canada. (Poster presentation)

5 **Q. Zheng**, I. Hasan, D. G. Sun, S. Abdul-Majid, and T. J. Hall, "Performance Comparison between Silicon-on-Insulator Curved Waveguides and Corner Turning Mirrors," *Photonic North 2011*, 16-18 May 2011, Ottawa, ON, Canada. (Oral presentation)

6 D. G. Sun, I. Hasan, S. Abdul-Majid, R. Vandusen, J. Udoeyop, **Q. Zheng**, A. Hussien, Z. Hu, G. Tarr, and T. J. Hall, "Performance Improvement to Silicon-on-Insulator Waveguide Directional Coupler based Devices," *Photonics Asia 2010*, 18-20 October 2010, Beijing, China.

7 K. Khan, **Q. Zheng**, D. Ioan, A. Benhsaien, S. Abdul-Mahid, Trevor J. Hall and Karin Hinzer, "O-band Semiconductor Optical Amplifier Design for CWDM Applications," *CMC 2010 TEXPO*, 4-6 October 2010, Ottawa, ON, Canada. (Conference abstract)

8 **Q. Zheng**, I. Hasan, D. G. Sun, S. Abdul-Majid, and T. J. Hall, "Performance Measurements of Silicon on Insulator Corner Turning Mirrors," *CMC 2010 TEXPO Research Competition*, 4-6 October 2010, Ottawa, ON, Canada. (Conference abstract)

5.3 Future Work

This thesis work has explored performance measurement of a few important SOI rib waveguide devices. Different measurement methods have been used to characterize the device response with the help of the Luna System. A complete testing setup has been built to perform the measurements. However, many challenges still remain in the measurement. For example, in the current measurement of phase behavior of the 4 × 4 MMI coupler, an optical fiber based delayed interferometer (Mach Zehnder type) has been built. Since the interferometer is inherently sensitive to environment changes, the measurement accuracy could be greatly affected. While the measurement time has been shortened to reduce the influence of environment disturbance, moderate errors are still observed over broad spectral range. Future research efforts could be made to develop a more stable measurement system. For example, integrating beam splitter, input optical waveguides and the 4×4 MMI device on a single chip will greatly improve the measurement accuracy. Such a device holds promise for coherent optical receiver systems where an optical 90^{o} hybrid is required.

LIST OF REFERENCE

[1] M. Lipson, "Guiding, modulating, and emitting light on silicon - Challenges and opportunities," *J. Lightwave Technol.,* vol. 23, no. 12, pp. 4222-4238, Dec. 2005.

[2] B. Jalali and S. Fathpour, "Silicon photonics," *J. Lightwave Technol.,* vol. 24, no. 12, pp. 4600-4615, Dec. 2006.

[3] V. R. Almeida, C. A. Barrios, R. R. Panepucci, and M. Lipson, "All-optical control of light on a silicon chip," *Nature,* vol. 431, no. 7012, pp. 1081-1084, Oct 28. 2004.

[4] L. Pavesi and D. Lockwood, *Silicon photonics*: Springer, 2004.

[5] R. A. Soref, J. Schmidtchen, and K. Petermann, "Large single-mode rib waveguides in GeSi-Si and Si-on-SiO₂," *Quantum Electronics, IEEE Journal of,* vol. 27, no. 8, pp. 1971-1974, 1991.

[6] R. A. Soref and J. P. Lorenzo, "All-Silicon Active and Passive Guided-Wave Components for Lambda=1.3 and 1.6 Mu-M," *Ieee J Quantum Elect,* vol. 22, no. 6, pp. 873-879, Jun. 1986.

[7] B. Schuppert, J. Schmidtchen, and K. Petermann, "Optical channel waveguides in silicon diffused from GeSi alloy," *Electron Lett,* vol. 25, no. 22, pp. 1500-1502, Oct. 1989.

[8] K. K. Lee, D. R. Lim, H. C. Luan, A. Agarwal, J. Foresi, and L. C. Kimerling, "Effect of size and roughness on light transmission in a Si/SiO2 waveguide: Experiments and model," *Appl Phys Lett,* vol. 77, no. 11, pp. 1617-1619, Sep 11. 2000.

[9] Y. Vlasov and S. McNab, "Losses in single-mode silicon-on-insulator strip waveguides and bends," *Opt. Express,* vol. 12, no. 8, pp. 1622-1631, 2004.

[10] M. Gnan, S. Thorns, D. S. Macintyre, R. M. De La Rue, and M. Sorel, "Fabrication of low-loss photonic wires in silicon-on-insulator using hydrogen silsesquioxane electron-beam resist," *Electron Lett,* vol. 44, no. 2, pp. 115-116, 2008.

[11] M. P. Nezhad, O. Bondarenko, M. Khajavikhan, A. Simic, and Y. Fainman, "Etch-free low loss silicon waveguides using hydrogen silsesquioxane oxidation masks," *Opt. Express,* vol. 19, no. 20, pp. 18827-18832, 2011.

[12] J. Cardenas, C. B. Poitras, J. T. Robinson, K. Preston, L. Chen, and M. Lipson, "Low loss etchless silicon photonic waveguides," *Opt Express,* vol. 17, no. 6, pp. 4752-4757, Mar 16. 2009.

[13] V. R. Almeida, R. R. Panepucci, and M. Lipson, "Nanotaper for compact mode conversion," *Opt. Lett.,* vol. 28, no. 15, pp. 1302-1304, Aug 1. 2003.

[14] A. S. Liu, R. Jones, L. Liao, D. Samara-Rubio, D. Rubin, O. Cohen, R. Nicolaescu, and M. Paniccia, "A high-speed silicon optical modulator based on a metal-oxide-semiconductor capacitor," *Nature,* vol. 427, no. 6975, pp. 615-618, Feb 12. 2004.

[15] L. Liao, D. Samara-Rubio, M. Morse, A. S. Liu, D. Hodge, D. Rubin, U. D. Keil, and T. Franck, "High speed silicon Mach-Zehnder modulator," *Opt Express,* vol. 13, no. 8, pp. 3129-3135, Apr 18. 2005.

[16] R. A. Soref and B. R. Bennett, "Electrooptical Effects in Silicon," *Ieee J Quantum Elect,* vol. 23, no. 1, pp. 123-129, Jan. 1987.

[17] L. Liao, A. Liu, D. Rubin, J. Basak, Y. Chetrit, H. Nguyen, R. Cohen, N. Izhaky, and M. Paniccia, "40 Gbit/s silicon optical modulator for highspeed applications," *Electron. Lett.,* vol. 43, no. 22, pp. 1196-1197, Oct 25. 2007.

[18] Y.-H. Kuo, Y. K. Lee, Y. Ge, S. Ren, J. E. Roth, T. I. Kamins, D. A. B. Miller, and J. S. Harris, "Strong quantum-confined Stark effect in germanium quantum-well structures on silicon," *Nature,* vol. 437, no. 7063, pp. 1334-1336, 2005.

[19] S. S. Iyer and Y. H. Xie, "Light-Emission from Silicon," *Science,* vol. 260, no. 5104, pp. 40-46, Apr 2. 1993.

[20] L. C. Kimerling, K. D. Kolenbrander, J. Michel, and J. Palm, "Light emission from silicon," *Solid State Phys,* vol. 50, pp. 333-381, 1997.

[21] T. Puritis and J. Kaupuzs, "Light emission from silicon nanocrystals," *Mater Sci Forum,* vol. 384-3, pp. 79-82, 2002.

[22] L. Dal Negro, J. H. Yi, L. C. Kimerling, S. Hamel, A. Williamson, and G. Galli, "Light emission from silicon-rich nitride nanostructures," *Appl Phys Lett,* vol. 88, no. 18, May 1. 2006.

[23] B. Goller and D. Kovalev, "Polarized red and blue light emission from silicon-based nanostructures correlated with crystallographic axes," *Phys Rev B,* vol. 83, no. 23, Jun 27. 2011.

[24] D. Liang and J. E. Bowers, "Recent progress in lasers on silicon," *Nature Photon.,* vol. 4, no. 8, pp. 511-517, Aug. 2010.

[25] M. H. Nayfeh, N. Barry, J. Therrien, O. Akcakir, E. Gratton, and G. Belomoin, "Stimulated blue emission in reconstituted films of ultrasmall silicon nanoparticles," *Appl Phys Lett,* vol. 78, no. 8, pp. 1131-1133, Feb 19. 2001.

[26] H. S. Rong, A. S. Liu, R. Jones, O. Cohen, D. Hak, R. Nicolaescu, A. Fang, and M. Paniccia, "An all-silicon Raman laser," *Nature,* vol. 433, no. 7023, pp. 292-294, Jan 20. 2005.

[27] O. Boyraz and B. Jalali, "Demonstration of a silicon Raman laser," *Opt. Express,* vol. 12, no. 21, pp. 5269-5273, Oct 18. 2004.

[28] A. Polman, G. N. Vandenhoven, J. S. Custer, J. H. Shin, R. Serna, and P. F. A. Alkemade, "Erbium in Crystal Silicon - Optical Activation, Excitation, and Concentration Limits," *J Appl Phys,* vol. 77, no. 3, pp. 1256-1262, Feb 1. 1995.

[29] A. W. Fang, H. Park, O. Cohen, R. Jones, M. J. Paniccia, and J. E. Bowers, "Electrically pumped hybrid AlGaInAs-silicon evanescent laser," *Opt. Express,* vol. 14, no. 20, pp. 9203-9210, Oct 2. 2006.

[30] A. Rickman, G. T. Reed, B. L. Weiss, and F. Namavar, "Low-loss planar optical waveguides fabricated in SIMOX material," *Photonics Technology Letters, IEEE,* vol. 4, no. 6, pp. 633-635, 1992.

[31] K. Okamoto, *Fundamentals of Optical Waveguides, 2nd Ed.*: Academic Press, 2006.

[32] A. M. Rossi, G. Amato, V. Camarchia, L. Boarino, and S. Borini, "High-quality porous-silicon buried waveguides," *Appl. Phys. Lett.,* vol. 78, no. 20, pp. 3003-3005, May 14. 2001.

[33] J. D. Joannopoulos, R. D. Meade, and J. N. Winn, *Photonic Crystals: Molding the Flow of Light*. Princeton, NJ: Princeton Univ. Press, 1995.

[34] C. Jamois, R. B. Wehrspohn, L. C. Andreani, C. Hermann, O. Hess, and U. Gösele, "Silicon-based two-dimensional photonic crystal waveguides," *Photonics and Nanostructures - Fundamentals and Applications,* vol. 1, no. 1, pp. 1-13, 2003.

[35] Q. F. Xu, V. R. Almeida, R. R. Panepucci, and M. Lipson, "Experimental demonstration of guiding and confining light in nanometer-size low-refractive-index material," *Opt. Lett.,* vol. 29, no. 14, pp. 1626-1628, Jul 15. 2004.

[36] G. J. Veldhuis, O. Parriaux, H. J. W. M. Hoekstra, and P. V. Lambeck, "Sensitivity enhancement in evanescent optical waveguide sensors," *J. Lightwave Technol.,* vol. 18, no. 5, pp. 677-682, May. 2000.

[37] G. T. Reed and A. P. Knights, *Silicon Photonics: An Introduction*: Wiley, 2004.

[38] J. B. Lasky, "Wafer Bonding for Silicon-on-Insulator Technologies," *Appl Phys Lett,* vol. 48, no. 1, pp. 78-80, Jan 6. 1986.

[39] B. Jalali, S. Yegnanarayanan, T. Yoon, T. Yoshimoto, I. Rendina, and F. Coppinger, "Advances in silicon-on-insulator optoelectronics," *Ieee J Sel Top Quant,* vol. 4, no. 6, pp. 938-947, Nov-Dec. 1998.

[40] M. W. Pruessner, T. H. Stievater, M. S. Ferraro, and W. S. Rabinovich, "Thermo-optic tuning and switching in SOI waveguide Fabry-Perot microcavities," *Opt Express,* vol. 15, no. 12, pp. 7557-7563, Jun 11. 2007.

[41] C. Z. Zhao, A. H. Chen, E. K. Liu, and G. Z. Li, "Silicon-on-insulator asymmetric optical switch based on total internal reflection," *Ieee Photonic Tech L,* vol. 9, no. 8, pp. 1113-1115, Aug. 1997.

[42] T. Maruyama, T. Okumura, S. Sakamoto, K. Miura, Y. Nishimoto, and S. Arai, "GaInAsP/InP membrane BH-DFB lasers directly bonded on SOI substrate," *Opt Express,* vol. 14, no. 18, pp. 8184-8188, Sep 4. 2006.

[43] K. K. Lee, D. R. Lim, L. C. Kimerling, J. Shin, and F. Cerrina, "Fabrication of ultralow-loss Si/SiO2 waveguides by roughness reduction," *Opt. Lett.,* vol. 26, no. 23, pp. 1888-1890, Dec 1. 2001.

[44] B. E. Little, J. S. Foresi, G. Steinmeyer, E. R. Thoen, S. T. Chu, H. A. Haus, E. P. Ippen, L. C. Kimerling, and W. Greene, "Ultra-compact Si-SiO2 microring resonator optical channel dropping filters," *IEEE Photon. Technol. Lett.,* vol. 10, no. 4, pp. 549-551, Apr. 1998.

[45] J. S. Foresi, P. R. Villeneuve, J. Ferrera, E. R. Thoen, G. Steinmeyer, S. Fan, J. D. Joannopoulos, L. C. Kimerling, H. I. Smith, and E. P. Ippen, "Photonic-bandgap microcavities in optical waveguides," *Nature,* vol. 390, no. 6656, pp. 143-145, Nov 13. 1997.

[46] T. K. Liang and H. K. Tsang, "Integrated polarization beam splitter in high index contrast silicon-on-insulator waveguides," *IEEE Photon. Technol. Lett.,* vol. 17, no. 2, pp. 393-395, Feb. 2005.

[47] C. A. Barrios, V. R. Almeida, R. Panepucci, and M. Lipson, "Electrooptic modulation of silicon-on-insulator submicrometer-size waveguide devices," *J. Lightwave Technol.,* vol. 21, no. 10, pp. 2332-2339, Oct. 2003.

[48] A. G. Rickman, G. T. Reed, and F. Namavar, "Silicon-on-insulator optical rib waveguide loss and mode characteristics," *J. Lightwave Technol.,* vol. 12, no. 10, pp. 1771-1776, 1994.

[49] S. P. Pogossian, L. Vescan, and A. Vonsovici, "The single-mode condition for semiconductor rib waveguides with large cross section," *J. Lightwave Technol.,* vol. 16, no. 10, pp. 1851-1853, 1998.

[50] O. Powell, "Single-mode condition for silicon rib waveguides," *J. Lightwave Technol.,* vol. 20, no. 10, pp. 1851-1855, 2002.

[51] P. K. Tien and R. Ulrich, "Theory of Prism-Film Coupler and Thin-Film Light Guides," *J. Opt. soc. Am.,* vol. 60, no. 10, pp. 1325-1337, 1970.

[52] R. M. Emmons and D. G. Hall, "Buried-Oxide Silicon-on-Insulator Structures .2. Wave-Guide Grating Couplers," *IEEE J. Quantum Electron.,* vol. 28, no. 1, pp. 164-175, Jan. 1992.

[53] G. Roelkens, D. V. Thourhout, and R. Baets, "High efficiency grating coupler between silicon-on-insulator waveguides and perfectly vertical optical fibers," *Opt. Lett.,* vol. 32, no. 11, pp. 1495-1497, 2007.

[54] D. Taillaert, H. Chong, P. I. Borel, L. H. Frandsen, R. M. De La Rue, and R. Baets, "A compact two-dimensional grating coupler used as a polarization splitter," *IEEE Photon. Technol. Lett.,* vol. 15, no. 9, pp. 1249-1251, Sep. 2003.

[55] Z. Sheng, D. X. Dai, and S. H. He, "Comparative Study of Losses in Ultrasharp Silicon-on-Insulator Nanowire Bends," *IEEE J. Sel. Topics Quantum Electron.,* vol. 15, no. 5, pp. 1406-1412, Sep-Oct. 2009.

[56] H. Srinivasan, B. Bommalakunta, A. Chamberlain, and J. T. Hastings, "Finite element analysis and experimental verification of SOI waveguide bending loss," *Microwave Opt. Tech. Lett.,* vol. 51, no. 3, pp. 699-702, 2009.

[57] Y. Z. Tang, W. H. Wang, T. Li, and Y. L. Wang, "Integrated waveguide turning mirror in silicon-on-insulator," *IEEE Photon. Technol. Lett.,* vol. 14, no. 1, pp. 68-70, Jan. 2002.

[58] S. Lardenois, D. Pascal, L. Vivien, E. Cassan, S. Laval, R. Orobtchouk, M. Heitzmann, N. Bouzaida, and L. Mollard, "Low-loss submicrometer silicon-on-insulator rib waveguides and corner mirrors," *Opt. Lett.,* vol. 28, no. 13, pp. 1150-1152, 2003.

[59] R. U. Ahmad, F. Pizzuto, G. S. Camarda, R. L. Espinola, H. Rao, and R. M. Osgood, Jr., "Ultracompact corner-mirrors and T-branches in silicon-on-insulator," *IEEE Photon. Technol. Lett.,* vol. 14, no. 1, pp. 65-67, 2002.

[60] Y. Okamura, S. Yoshinaka, and S. Yamamoto, "Measuring mode propagation losses of integrated optical waveguides: a simple method," *Appl. Opt.,* vol. 22, no. 23, pp. 3892-3894, 1983.

[61] D. Castaldini, P. Bassi, S. Tascu, G. Sauder, P. Aschieri, M. De Micheli, P. Baldi, K. Thyagarajan, and M. R. Shenoy, "All-in-one measurement setup for fast and accurate linear characterization of guided-wave optical devices," *Opt. Eng.,* vol. 46, no. 12, Dec. 2007.

[62] I. P. Kaminow and L. W. Stulz, "Loss in Cleaved Ti-Diffused Linbo3 Waveguides," *Appl. Phys. Lett.,* vol. 33, no. 1, pp. 62-64, 1978.

[63] S. Taebi, M. Khorasaninejad, and S. S. Saini, "Modified Fabry-Perot interferometric method for waveguide loss measurement," *Appl. Opt.,* vol. 47, no. 35, pp. 6625-6630, 2008.

[64] A. De Rossi, V. Ortiz, M. Calligaro, L. Lanco, S. Ducci, V. Berger, and I. Sagnes, "Measuring propagation loss in a multimode semiconductor waveguide," *J Appl Phys,* vol. 97, no. 7, Apr 1. 2005.

[65] G. D. VanWiggeren, A. R. Motamedi, and D. M. Baney, "Single-scan interferometric component analyzer," *IEEE Photon. Technol. Lett.,* vol. 15, no. 2, pp. 263-265, Feb. 2003.

[66] U. Glombitza and E. Brinkmeyer, "Coherent frequency-domain reflectometry for characterization of single-mode integrated-optical waveguides," *J. Lightwave Technol.,* vol. 11, no. 8, pp. 1377-1384, 1993.

[67] K. Ogusu, "Transmission characteristics of optical waveguide corners," *Opt. Commun.,* vol. 55, no. 3, pp. 149-153, 1985.

[68] J. Čtyroký, H. Hoekstra, G. J. M. Krijnen, P. V. Lambeck, L. Joannes, D. Decoster, A. P. Leite, R. Pregla, E. Ahlers, J. F. Vinchant, and M. A. Andrade, "Modelling of self-aligned total internal reflection waveguide mirrors: an interlaboratory comparison," *Opt. Quant. Electron.,* vol. 27, no. 10, pp. 935-942, 1995.

[69] D. G. Sun, X. Q. Li, D. X. Wong, Y. Hu, F. L. Luo, and T. J. Hall, "Modeling and Numerical Analysis for Silicon-on-Insulator Rib Waveguide Corners," *J. Lightwave Technol.,* vol. 27, no. 20, pp. 4610-4618, Oct 15. 2009.

[70] I. E. Johnson and C. L. Tang, "Precise determination of turning mirror loss using GaAs/AlGaAs lasers with up to ten 90 degrees intracavity turning mirrors," *IEEE Photon. Technol. Lett.,* vol. 4, no. 1, pp. 24-26, 1992.

[71] R. Ulrich, "Image-Formation by Phase Coincidences in Optical-Waveguides," *Opt. Commun.,* vol. 13, no. 3, pp. 259-264, 1975.

[72] T. Niemeier and R. Ulrich, "Quadrature Outputs from Fiber Interferometer with 4x4 Coupler," *Opt. Lett.,* vol. 11, no. 10, pp. 677-679, Oct. 1986.

[73] D. Hoffman, H. Heidrich, G. Wenke, R. Langenhorst, and E. Dietrich, "Integrated optics eight-port 90 degrees hybrid on $LiNbO_3$," *J. Lightwave Technol.,* vol. 7, no. 5, pp. 794-798, 1989.

[74] C. R. Doerr, P. J. Winzer, C. Young-Kai, S. Chandrasekhar, M. S. Rasras, C. Long, L. Tsung-Yang, A. Kah-Wee, and L. Guo-Qiang, "Monolithic Polarization and Phase Diversity Coherent Receiver in Silicon," *J. Lightwave Technol.,* vol. 28, no. 4, pp. 520-525, 2010.

[75] S.-H. Jeong and K. Morito, "Optical 90° hybrid with broad operating bandwidth of 94 nm," *Opt. Lett.,* vol. 34, no. 22, pp. 3505-3507, 2009.

[76] M. Bachmann, P. A. Besse, and H. Melchior, "General self-imaging properties in N × N multimode interference couplers including phase relations," *Appl. Opt.,* vol. 33, no. 18, pp. 3905-3911, 1994.

[77] E. C. M. Pennings, R. J. Deri, R. Bhat, T. R. Hayes, and N. C. Andreadakis, "Ultracompact, all-passive optical 90 degrees -hybrid on InP using self-imaging," *IEEE Photon. Technol. Lett.,* vol. 5, no. 6, pp. 701-703, 1993.

[78] L. Zimmermann, K. Voigt, G. Winzer, K. Petermann, and C. M. Weinert, "C-Band Optical 90-degree Hybrids Based on Silicon-on-Insulator 4 x 4 Waveguide Couplers," *IEEE Photon. Technol. Lett.,* vol. 21, no. 3, pp. 143-145, 2009.

[79] S. Abdul-Majid, I. I. Hasan, P. J. Bock, and T. J. Hall, "Design, simulation, and fabrication of a 90° SOI optical hybrid based on the self-imaging principle," in *Proc. SPIE*, 2010, p. 77190E.

[80] M. Takeda, H. Ina, and S. Kobayashi, "Fourier-Transform Method of Fringe-Pattern Analysis for Computer-Based Topography and Interferometry," *J. Opt. soc. Am.,* vol. 72, no. 1, pp. 156-160, 1982.

[81] H. Emami, N. Sarkhosh, L. A. Bui, and A. Mitchell, "Amplitude independent RF instantaneous frequency measurement system using photonic Hilbert transform," *Opt. Express,* vol. 16, no. 18, pp. 13707-13712, Sep 1. 2008.